Technische Universität Berlin

Institut für Luft- und Raumfahrt
Fachgebiet Raumfahrttechnik

Fakultät V
Marchstraße 12-14
10587 Berlin
https://www.ilr.tu-berlin.de

Master's Thesis

GNSS-based Position and Baseline Determination and Simultaneous Clock Synchronization for Multistatic Synthetic Aperture Radar Constellations

Eduardo Rodrigues Silva Filho

Matriculation Number: 399232
19.06.2020

Supervised by
Prof. Dr. Klaus Brieß

Assistant Supervisor
Clément Jonglez

Acknowledgments

This dissertation originated from nine months of research at the Microwave and Radar Institute of the German Aerospace Center (DLR). First of all, I owe my gratitude to Dr. Marc Rodriguez Cassola for the opportunity to carry out research at DLR, for proposing this fascinating research topic, and for all his guidance and support. I would also like to thank Prof. Dr.-Ing. Gerhard Krieger for his valuable feedback and suggestions. I would furthermore like to thank my co-supervisor Clément Jonglez for his many suggestions which helped me to improve and polish the thesis. Finally, I would like to thank my family for the constant and unconditional support during this master's program.

Berlin, 19.06.2020
Eduardo Rodrigues Silva Filho

Hereby I declare that I wrote this thesis myself with the help of no more than the mentioned literature and auxiliary means.

Berlin, 19.06.2020

Eduardo Rodrigues Silva Filho

Signature

Abstract

Satellite formation flying allows for many innovative mission concepts which can sometimes better perform than missions based on single large satellites. They also offer several advantages, among which are the reduced cost and risk due to the distributed architecture and smaller, simpler spacecraft design. One possible application of such mission designs consists in deploying several small Synthetic Aperture Radar (SAR) satellites flying in close formation. SAR images of metric and submetric resolution can be synthesized by combining the data from several small spacecraft. The feasibility of such multistatic SAR mission concepts largely relies on the ability to achieve relative time and phase synchronization accuracy better than a few picoseconds and a few degrees, respectively. The proposed master thesis provides an overview, including preliminary performance assessment, of the following aspects in the frame of multistatic constellations: i) improvement of positioning accuracy, ii) improvement of relative positioning (i.e., baseline) accuracy, and iii) GNSS-based clock synchronization.

This work proposes joint kinematic estimators combining code delay GNSS data from satellites in close formation (tens of meters) with different hardware configurations. The thesis evaluates the effects of combining single and dual-frequency receivers and of adding an intersatellite ranging system to a pair of satellites in the formation. In addition, it proposes and evaluates an algorithm using information derived from SAR interferometry to calibrate the baselines. A simulator for the GNSS data and for the interferometric and intersatellite ranging data was developed for testing the algorithms. The comparative results indicate improvement in the baseline estimates by employing data from an intersatellite ranging system and also by using the calibration algorithm based on interferometric data. The position estimates improved with the number of satellites in the formation in the scenario where each satellite is equipped with a dual-frequency receiver. Finally, dual frequency receivers could be used to improve baseline and positioning results for single frequency receivers by estimating the ionospheric delay affecting the whole formation.

This thesis also puts forward a phase synchronization scheme based on the combined evaluation of precise orbit determination (POD) and GNSS data, in which the GNSS receiver and the radar payload share the same oscillator. It presents a discussion on accuracy, an error analysis, and an evaluation of its viability by means of a system-oriented simulation of the navigation data. The results suggest the proposed approach is capable of delivering reliable estimates of carrier frequency and phase errors for low- and medium-frequency systems in the absence of strong baseline velocity deviations if multipath and other systematic errors are successfully suppressed or calibrated.

Contents

List of Figures

List of Tables

List of Acronyms

CW	Clohessy-Wiltshire
DEM	Digital Elevation Model
DLR	Deutsche Zentrum für Luft- und Raumfahrt
ECI	Earth Centered Inertial
GLONASS	Global'naya Navigatsionnaya Sputnikovaya Sistema
GMAT	General Mission Analysis Tool
GNSS	Global Navigation Satellite System
GPS	Global Positioning System
GSOC	German Space Operations Center
LEO	Low Earth Orbit
MEO	Medium Earth Orbit
NASA	National Aeronautics and Space Administration
POD	Precise Orbit Determination
PRN	Pseudo-Random Noise
RAR	Real Aperture Radar
SAR	Synthetic Aperture Radar
STK	Systems Tool Kit
TEC	Total Electron Content
TLE	Two-Lines Element set
USO	Ultra Stable Oscillator
VTEC	Vertical Total Electron Content

1 Introduction

1.1 Motivation

Synthetic Aperture Radar is one of the most powerful remote sensing techniques available. One of the main features of radar remote sensing in general is that it provides high-resolution two dimensional images which do not depend on daylight or weather conditions, thus offering a reliable means of monitoring the dynamic processes of the Earth. Radar systems measure the distance to an object by observing the time interval and the phase difference between a transmitted microwave signal and its received echo. The simplest radar applications provide a 2-D reflectivity map of the imaged area. Synthetic Aperture Radars (SAR) consist of conventional radars mounted on a moving platforms. In these systems, the antenna displacement between the times of transmission and reception allows for the construction of an aperture larger than the antenna length by coherently combining the received signals [MPY^{+}13]. One SAR application of particular interest in this thesis is the so-called across-track interferometry, in which two antennas are laterally displaced and the combination of their two images gives information on the imaged surface elevation.

In conventional radar systems the transmitter and receiver are on the same platform. In bistatic and multistatic space radar systems they are spatially separated, which typically reduces development costs and risks, and enhances the overall performance [KM06]. Multistatic radar constellations also allow for better reconfigurability and scalability. A system composed of a combination of small standard satellites is easier to reconfigure and, depending on the system design, the performance could be scaled with the number of satellites without the need for changing each of them. Bistatic systems provide additional observables, enabling the extraction of important parameters from the scene. A multistatic system with several satellites illuminating a common footprint can be considered as a large aperture system, which results in a very narrow antenna beam and allows for reducing the size of each antenna, thus enabling cost-effective high-resolution SAR missions [KM06].

In bistatic and multistatic systems, however, different oscillators are used for modulation and demodulation of the radar signal, and the low-frequency part of the phase noise process cannot be expected to cancel out as in monostatic systems [Aut84]. This residual phase may cause defocusing, position and phase errors in the computed images, which may compromise the use of the systems for interferometric and tomographic applications [KY06].

Another challenge for designing bistatic and multistatic radar systems is the very high accuracy required in determining the baseline, which is the relative position between the

Figure 1.1: TandemX artistic concept (credits: DLR).

transmitter and receiver antennas. A very high accuracy, of the order of millimeters or even sub-millimeter level, can be achieved by using geodetic grade GNSS receivers and precise orbit and baseline determination techniques. Future radar applications for small satellites could benefit from estimation techniques that improve the baseline accuracy, specially if they can be used with data from low-cost, small GNSS receivers.

The TanDEM-X mission, illustrated in fig. 1.1, exemplifies the stringent requirements for interferometric bistatic missions. It was launched in 2010 and consists of two satellites flying in a controlled helix formation with the objective of generating a digital elevation model of the Earth with the unprecedented accuracy of 2 m. The generation of high-resolution digital elevation models required the knowledge of relative phases within a few degrees [KMF$^+$07] and the baselines needed to be determined within 1-2 millimeter accuracy to allow for the targeted relative height accuracy [GAB$^+$12].

In TanDEM-X, phase synchronization with the required accuracy was achieved by exchanging compressed pulses at the radar carrier frequency between the satellites through a direct microwave link [BV], which involved the implementation of dedicated transmit and receive hardware and a total of six antennas covering most of the angular environment of the satellites. Besides the need for additional hardware, the incorporation of such direct links may be problematic due to differences in the development schedules of different elements of the constellation, as it is typically the case of companion SAR missions [RCPIZ+17].

Another possibility would be to estimate the synchronization phase based on the evaluation of the received data. Although this approach was demonstrated in spaceborne environments [RCPS+12, RC12] and it provides estimates with varying quality as a function of the backscattering of the scene, it can only be considered acceptable for interferometric SAR missions.

In an attempt to fulfill the phase synchronization requirement in a most cost-effective manner, in [KZM+18] a full system architecture (MirrorSAR) is envisaged to avoid the demodulation of the radar signals using a different oscillator. The approach consists of having the receivers act like transponders, i.e., re-routing the radar echoes to another element of the constellation (e.g., the transmitter) having access to the oscillator used in the modulation. Although a MirrorSAR architecture requires a direct link between the satellites, not necessarily in the microwave range, it still keeps the potential for relevant spacecraft simplification by an appropriate design of baselines and the possible removal of complete hardware blocks for demodulation, data storage, downlink or digital control in the receivers.

The capability of high accuracy relative positioning (i.e., baseline determination) and timing using GNSS has been extensively demonstrated in space. The baseline determination required in TanDEM-X was achieved through *a posteriori* calibration based on the evaluation of the raw topographic maps of several sites spread across the world acquired under different geometries [GAB+12]. GRACE achieved an accuracy of 1 mm with respect to the more precise K-band ranging system, used as reference [KMBV05]. Both missions used geodetic GPS receivers, capable of receiving two frequencies for correcting the effects of the ionosphere. The PRISMA mission, on the other hand, demonstrated the capability of achieving sub-decimeter relative positioning precision using a low-cost single frequency GPS receiver [ADM10].

In the standard navigation solution the phase drift of the oscillator used in the GNSS receiver directly affects the pseudorange measurements between the GNSS satellite and the GNSS receiver and thus has to be estimated along with the position and velocity in a filter. The phase estimated in the filter gives information on the accumulated phase error due to frequency deviations on the master oscillator of the GNSS receiver. This indicates the possibility of a phase synchronization method using precise baseline determination and in which the same master oscillator is shared between the GNSS receiver and the radar payload.

1.2 Objective

This thesis evaluates some of the potentials of GNSS applications for multistatic SAR constellations. It addresses the issue of precise phase synchronization and precise baseline determination having as a vision a multistatic SAR constellation consisting of several low-cost small satellites. The developments presented here, however, could also be useful for conventional bi- and multistatic SAR missions.

The first major objective of this thesis is to investigate if data from multiple satellites flying in close formation can be combined to achieve more accurate baseline solutions. This preliminary assessment covers the basic cases in which each satellite is provided with a double-frequency GNSS receiver, and considers the effect on the position and baseline solutions when other information is added to the estimator. The thesis evaluates the effect of intersatellite links, different capabilities of each GNSS receiver in terms of frequency, and the possibility of using interferometric SAR data from different pairs of satellites to calibrate the baseline.

The second major objective is to propose and evaluate a relative SAR carrier phase estimator for bi- and multistatic SAR constellations in a hypothetical system in which the radar payload and the navigation receiver share the same master oscillator, exploiting the fact that the phase drift of the oscillator needs to be estimated in the standard navigation solution.

1.3 Scope

The position and baseline determination are evaluated in a preliminary fashion. A kinematic solution, which does not consider in the estimation the spacecraft orbital dynamics, is enough to evaluate if the information content of the GNSS signals in different satellites combined with other external information sources can be used to improve the baseline configuration. The basic assumption is that if there is no improvement in the baseline for the kinematic solution, the dynamic solution will not be improved either and, on the other hand, if there is an improvement, it would indicate that the final solution using a dynamic solution could improve.

The phase determination problem will be presented in detail. The intention is to propose an estimator and to provide a simulation to assess the performance of the proposed synchronization scheme in as much detail as possible. The error sources are listed and analyzed individually in terms of order of magnitude and variation over time. Analytical expressions for some of the major errors sources are derived.

1.4 Outline

The chapters are divided into two major themes: position and baseline determination, and SAR synchronization, with dedicated chapters for each. The thesis is separated into seven chapters, including this introduction:

Chapter 2 exposes the fundamentals of position determination and SAR phase synchronization and sets the basic theoretical framework and notations for the following chapters.

Chapter 3 first details all the kinematic position determination configurations considered and the mathematical models used in the kinematic estimator for each of them. Then, it gives an overview of the simulation developed to evaluate those algorithms and finally presents the results from the simulation.

Chapter 4 proposes and details a technique for estimating the phase difference between radar payloads using GNSS and POD data and gives an analytical error analysis for the proposed technique. It shows the simulation framework and the assumptions to assess the performance of the proposed phase estimator for a system example.

Chapter 5 summarizes the conclusions, describes the non-addressed issues which may cause problems for the implementation in the future and proposes the next step to further assess the technique and to take it into the practical implementation.

2 Fundamentals

This section gives an introduction on two major themes: SAR remote sensing and GNSS navigation. It explains the most relevant concepts on which the developments throughout the thesis are based and introduces the main terms and mathematical notations. This chapter gives a brief understanding on each concept necessary, avoiding lengthy derivations. For more detailed information, refer to [CW05] and [MG00], which are more comprehensive references on SAR remote sensing and navigation, respectively. The notations and equations concerning GNSS navigation used here are largely based on the PhD thesis by Remco Kroes [Kro06].

2.1 Synthetic Aperture Radar

Initially, radar remote sensing systems did not use the principle of the synthetic aperture, and had the drawback of limited resolution in one of the image dimensions, namely the azimuth direction. In 1951 Carl Wiley invented the use of coherent radar and the principle of Doppler beam sharpening, which lead to improvement on azimuth resolution and resulted in the concept of synthetic aperture radar used nowadays.

The initial developments of SAR were mainly targeted at military applications, such as reconnaissance and man-made target detection. In the 70s and 80s many airborne systems for civilian applications were developed with the goal of retrieving geo/bio-physical parameters. In 1978 the Jet Propulsion Lab from NASA launched the first civilian SAR satellite, named Seasat, which measured various sea and atmosphere parameters. Nowadays, SAR is established as one of the most important remote sensing techniques, being able to provide images with resolutions on the order of meters. The field of SAR remote sensing is also following the current trend of using small satellites. Recently, the microsatellite missions ICEYE were able to achieve resolution on the order of a few meters [ece].

The next subsection explains the general principles of real and synthetic aperture remote sensing. The following two subsections explain the basics of phase synchronization and across-track interferometry for SAR applications.

2.1.1 Synthetic Aperture Radar Principle

In order to understand the SAR principle, it is important to understand the limitations on the simplest radar imaging system as it was conceived initially. These systems are currently denominated Real Aperture Radar (RAR), since they do not use the principle of synthetic aperture radar. The principle of RAR is illustrated in Fig. 2.1.

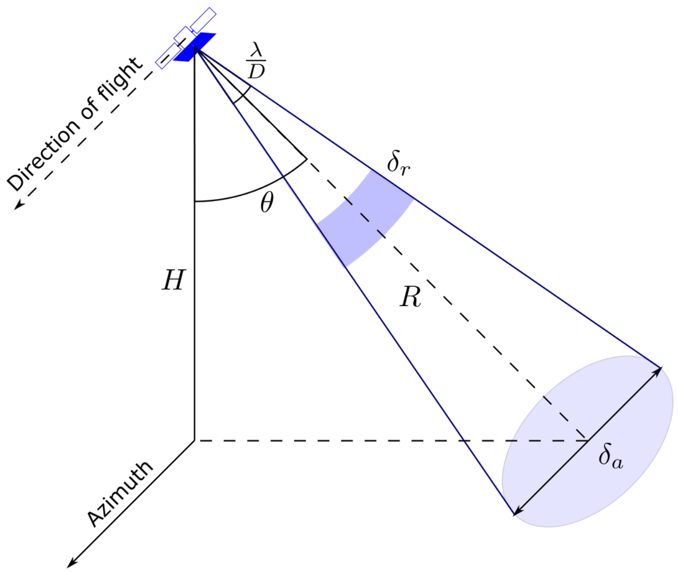

Figure 2.1: Real Aperture Radar (RAR) remote sensing principle.

The RAR system provides a 2-D reflectivity map of the scenery, in which areas or targets with high backscattering are represented as bright spots, and flat smooth surfaces are represented as dark areas. The image is built in the direction of flight, denominated azimuth direction, and along the line-of-sight, denominated slant range direction. Radar sensors send frequency modulated pulse waveforms, the so-called *chirp* signal, and waits for a period in which the radar receives the scattered echoes and stores the signal on-board.

The resolution corresponds to the smallest distance between two points in the scenery which can be detected by the radar. The beamwidth in the azimuth direction Θ_a is given by

$$\Theta_a = \frac{\lambda}{D}\,, \tag{2.1}$$

in which λ is the wavelength and D is the antenna length. From Fig. (2.1), and considering $\tan(\Theta_a) \approx \Theta_a$, valid for small Θ_a, the resolution in azimuth is given by

$$\delta_a = \Theta_a \cdot R = \frac{\lambda}{D} \cdot R\,, \tag{2.2}$$

in which R is the range distance from the antenna to the target. Eq. 2.2 shows that the azimuth resolution decreases with the distance to the target. This restricts the performance in azimuth of spaceborne RAR systems to low to average resolution.
The resolution in slant range direction depends on the pulse duration τ as follows [CW05]:

$$\delta_r = \frac{c \cdot \tau}{2 \cdot \sin(\theta)}\,, \tag{2.3}$$

with θ the look angle as illustrated in Fig. 2.1 and c the speed of light. Note that there is a singularity for $\theta = 0$, but it poses no problem since θ must be always positive to avoid ambiguity in the radar data between signals received from the left and from the right of the direction of flight. The resolution in slant range does not degrades with the distance and tends to be much higher than the resolution in azimuth for these systems.

For example, consider a theoretical spaceborne RAR system with 1 cm wavelength, 5 m antenna length, at an altitude of 600 km, incident angle of 59 degrees and range of 1000 km. The resolution in slant range would be of 5.2 meters whereas the resolution in azimuth would be of 2.3 km, a very large difference.

The principle of synthetic aperture radar, which addresses this discrepancy between resolutions, is illustrated in Fig. 2.2.

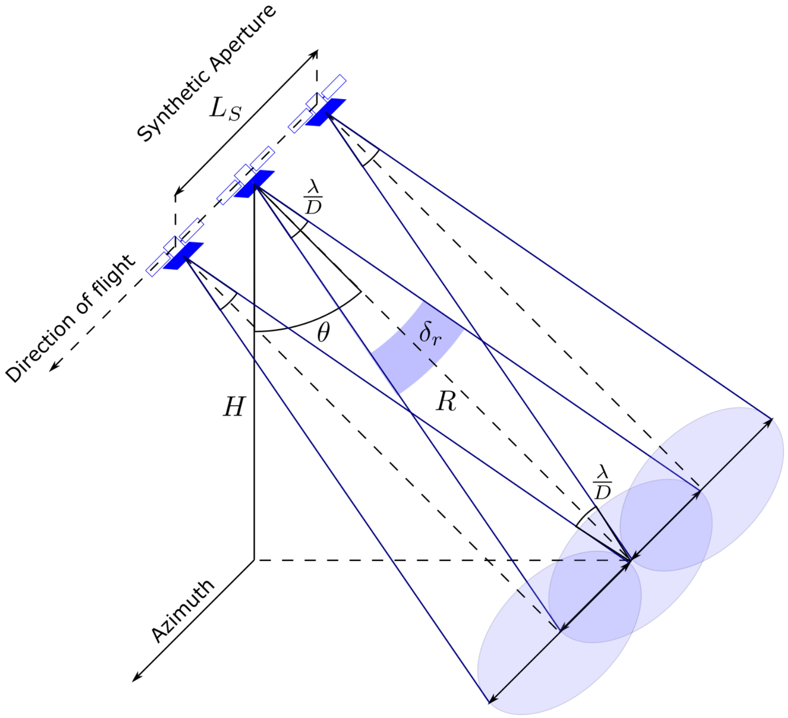

Figure 2.2: Synthetic Aperture Radar principle.

In these radar systems a common point is illuminated from different azimuth positions. The azimuth resolution is determined by the constructed synthetic aperture, defined as the length of the trajectory segment during which a point is illuminated by the radar. As shown in Fig. 2.2, the synthetic aperture L_s is given by

$$L_s = \Theta_a \cdot R = \frac{\lambda R}{D}\,. \tag{2.4}$$

This long aperture results in a narrow virtual beamwidth (Θ_{sa}), as shown in the equation

$$\Theta_{sa} = \frac{\lambda}{2 \cdot L_s} = \frac{D}{2 \cdot R}, \tag{2.5}$$

and consequently on a high azimuth resolution

$$\delta_a = R \cdot \Theta_{sa} = \frac{D}{2}. \tag{2.6}$$

For SAR systems, therefore, the resolution in azimuth doesn't depend on the slant distance and can be of the order of meters, many orders of magnitude lower than the resolution provided by a spaceborne RAR. For the same theoretical mission presented earlier in this subsection, if SAR was used instead of RAR, the resolution in azimuth direction would be of 2.5 m, almost a thousand times better than the 2.3 km resolution of the RAR system.

2.1.2 Synthetic Aperture Radar Data Processing

The data from a SAR payload consists in a two-dimensional matrix containing the complex received signals, with information of amplitude and phase. The first dimension corresponds to the range direction. Each range line contains the received echo after amplification, conversion to base band and digitization. The second dimension is the traveled distance in the direction of flight.

Differently from optical data, the raw SAR data cannot be directly interpreted. The data has to go through a complex data processing before it can be translated into an image. In a simplified way, the data processing can be understood as a sequence of two separate matched filters operations, one in the range direction followed by one in the azimuth direction.

In the matched filter the received signal is convoluted with a template, consisting in the complex conjugate of the original signal. In the first matched filter the received signal is convoluted with the transmitted chirp. The result is a range-compressed image, which reveals only the relative distance between the radar and any point on the ground. In the second matched filter the azimuth information is retrieved by multiplying the range-compressed image by the complex conjugate of a model of the expected signal received from any target point at a given range. The reference azimuth signal can be modeled as follows

$$s(t) = A \cdot \sqrt{\sigma_0} \cdot \exp\left(j\phi^{scatt}\right) \cdot \exp\left(-j2\pi f_r \tau\right), \tag{2.7}$$

in which j is the imaginary unit, f_r is the radar frequency, σ_0 is the radar cross section, ϕ^{scatt} is the scatterer phase, τ is the wave traveled time from transmission to reception, and A expresses the dependency of the received signal amplitude on system parameter such as transmit power, antenna pattern, azimuth and elevation angle. The component $2\pi f_r \tau$ is the azimuth phase variation due to the traveled distance. This component plays a central role in the problem addressed by this thesis, as will be explained in details in the next section.

2.1.3 Bistatic Phase Synchronization

The azimuth modulation expressed in 2.7 is directly affected by variations in the oscillator originating the signal. Fig. 2.3 illustrates the effect of drifts in the oscillator in the case of a monostatic radar system, in which the signal is transmitted and demodulated using signals generated from the same oscillator.

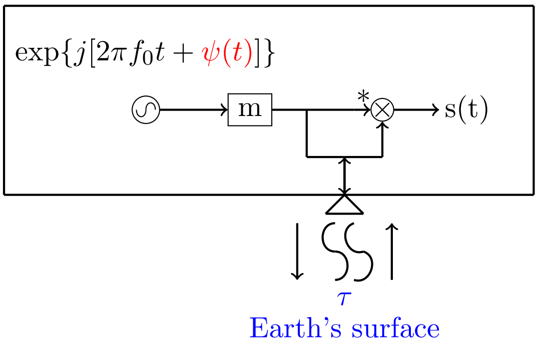

$$s(t) = \exp\{jm[\underbrace{-2\pi f_0 \tau}_{\text{AZ modulation}} + \underbrace{\psi(t-\tau) - \psi(t)}_{\text{phase error} \approx 0}]\}$$

Figure 2.3: Monostatic SAR phase error.

In this figure the amplitude information is ignored and just the phase information is expressed. The radar signal is generated by a oscillator signal and a frequency multiplier. It puts in evidence an phase error which is not accounted for in Eq. (2.7) and which gets mixed with the azimuth phase variation, ultimately introducing errors in the final synthesized SAR image. In the case shown in Fig. 2.3 the errors caused by the oscillator is negligible, provided that the phase error bias of the oscillator doesn't change considerably in the interval of time τ, and thus cancels out when recombining it with the template.

In the case of a bistatic system this scenario changes. In these systems different oscillators are use for modulation and demodulation and therefore this phase in general will not cancel out. This is illustrated in Fig. 2.4. This error mixes up with the azimuth information and will cause several distortions in the synthesized image if not properly compensated. This is one of the main challenge for the implementation of bistatic and multistatic SAR systems. Fig. 2.5 exemplifies the effect of the phase error for a SAR interferogram, built through across-track interferometry and which gives elevation information about an area.

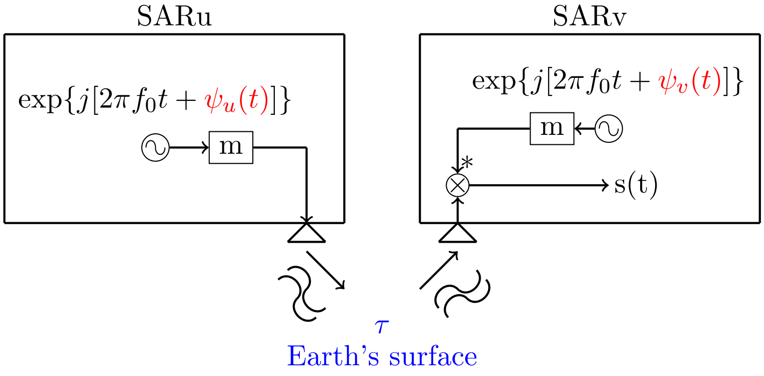

$$s(t) = \exp\{jm[\underbrace{-2\pi f_0\tau}_{\text{AZ modulation}} + \underbrace{\psi_u(t-\tau) - \psi_v(t)}_{\text{phase error}}]\}$$

Figure 2.4: Bistatic SAR phase error.

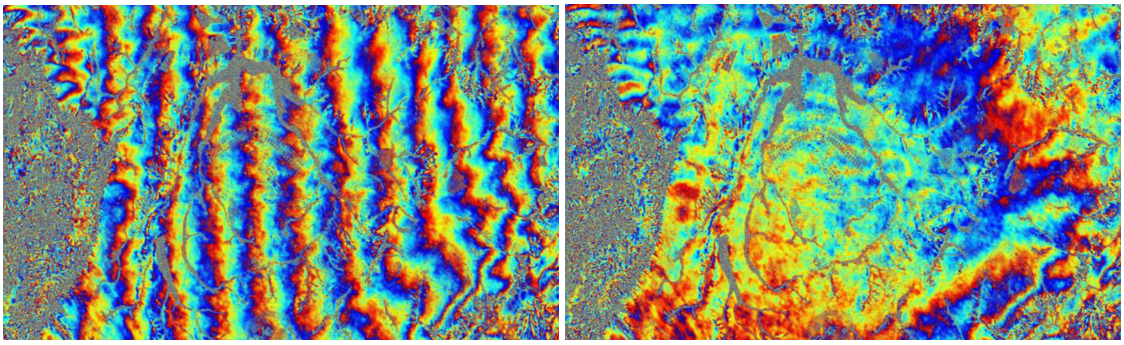

Figure 2.5: Bistatic interferograms of Brasilia area from TanDEM-X mission. At left a non-synchronized and at right a synchronized interferogram (source: DLR).

2.1.4 Across-Track Interferometry

One of the main applications of bi-static SAR is the so called across-track interferometry. The conventional radar image provides information on the range and elevation of certain pixel, but not the elevation and therefore the height of that pixel. The across-track interferometry overcomes this limitation by comparing two radar images of the same area taken from a laterally displaced antenna, as illustrated in Fig. 2.6.

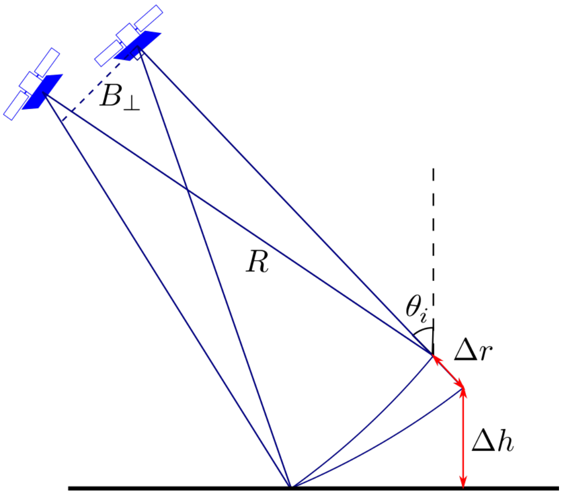

Figure 2.6: Across-Track Interferometry principle.

The variation in height can be derived from the variation in range as follows

$$\Delta r = \frac{B_\perp}{R\sin(\theta_i)} \cdot \Delta h \,. \tag{2.8}$$

This technique allows for building a digital elevation model (DEM) of the imaged terrain, in addition to the reflectivity map. An error in the baseline will result in an error in the estimated elevation and a distortion of the elevation model. This is further explained in [GAB$^+$12].

2.2 GNSS Navigation

Global Navigation Satellite Systems (GNSS) are constellations of satellites that provide positioning and timing information at a global scale. The GNSS systems consists of three major segments: space segment, which are the satellites of the constellation, the ground segment, consisting of the control and tracking ground stations and the user segment.

The first developed GNSS was the NAVSTAR GPS (NAVigation System and Ranging Global Positioning), which was initiated in 1973 and achieved its full operational capacity on 1995. The GPS system consists of 24 satellites placed in six evenly spaced planes with 55 degrees inclination and four satellites per plane. It is developed, maintained and operated by the U.S. Air Force. Currently there are several additional GNSS systems available, from different countries, including Europe's Galileo, Russia's Global'naya Navigatsionnaya Sputnikovaya Sistema (GLONASS) and China's BeiDou Navigation Satellite System.

In these systems, each satellite transmit L-band signals modulated with pseudo-range codes used for acquisition and tracking of the satellites. The three main components of the GNSS signal are: the carrier frequency, a sinusoidal signal at a central frequency;

the navigation data, a binary-coded message providing the GNSS satellite ephemerides, clock bias parameters, satellite health status, among others; and finally, the so-called Pseudo-Random Noise (PRN) sequence, a binary sequence which allow to determine the travel time of the signal from the GNSS satellite to the receiver.

Each GNSS constellation transmits continuously at least two of the signals described above at two separate carrier frequencies. The use of two frequencies allows for the correction of the main error source in GNSS positioning, the ionospheric delay.

The following subsections detail the GNSS positioning principle, followed by a mathematical description of the useful observables extracted from the GNSS signal, and finally it presents a algorithm for position estimation based on these observables.

2.2.1 GNSS Navigation Principle

Figure 2.7 illustrates the principle of GNSS navigation. The positioning is based on triangulation from four satellites with known positions. Assuming the clocks between the GNSS satellites and the receiver are synchronized, the distances from the satellites to the receiver can be determined directly from the code delay information contained in the signal.

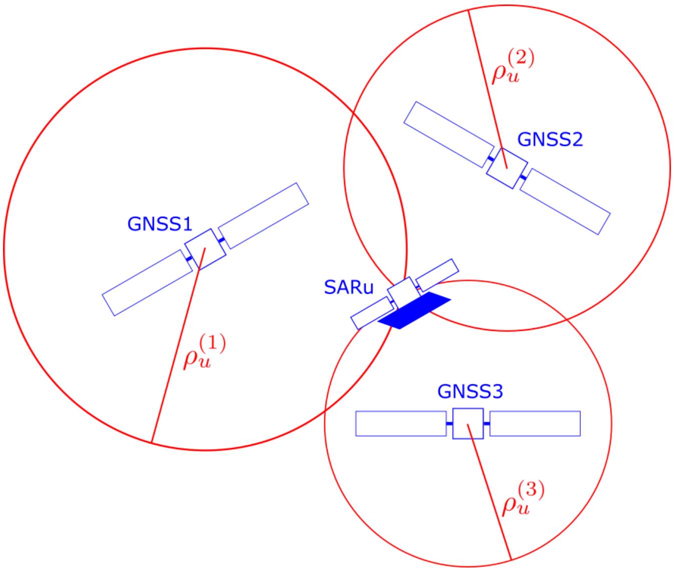

Figure 2.7: GNSS position simplified principle.

From this distance information, the user knows that they are somewhere in a sphere centered on the GNSS position of radius equal to the measured distance. Each GNSS satellite provides one sphere of possible location, and the user can determine its position by calculating the interception point between those spheres. The position information consists of three independent pieces of information, therefore at least three independent measurements are necessary for calculating the position.

In case the clocks are not synchronized, the clock bias would be interpreted as a range information in the algorithm, which would result in a erroneous position if the delay is not considered. Therefore, along with the satellite position, the clock bias has to be estimated in the solution. Because the range information derived from the code in the GNSS signal is biased with the clock differences, it is denominated pseudorange. Assuming the GNSS satellites are synchronized between each other, this bias adds an additional variable to be estimated. Therefore four variables must be calculated and thus four measurements are necessary. With the signals from four GNSS satellite the clock bias and the position of the user can be determined.

The model described above is a simplification of the GNSS positioning principle. In practice, error sources will affect the positioning and have to be accounted for, either by calibrating the data or by modeling the additional effects and estimating them along with the position and clock bias from the data. The next section gives the models for the GNSS observable pseudorange data including the main error sources.

2.2.2 GNSS observables

The GNSS receiver provides two observables. The first is the already mentioned code delay, an absolute estimate of the distance between the GNSS satellite and the receiver biased by a clock error. The second measurement is the signal carrier phase. At the instant the receiver starts tracking a GNSS satellite, it records an initial phase and the variations from this phase during the whole tracking period. This measurement is not limited to the interval from 0 to 2π since the receiver can record the integer number of cycles passed. The measured phase, when multiplied by the wavelength, corresponds to a range value with respect to the moment at which the phase was acquired. In order to determine the range from the receiver to GNSS satellite from the phase estimate, an additional constant, named ambiguity, must be determined. This constant accounts for the integer number of wavelengths between the GNSS and the receiver at the time the satellite was started being tracked. The phase delay, despite imposing the additional difficulty of determining the ambiguities, has a noise level several orders of magnitude lower than the code delay, and allows for much more precise estimates. This is the reason why the phase information and the ambiguity resolution are crucial for precise orbit determination algorithms.

In the case of spacecrafts, the larger contributor to the positioning errors is the delay on the signal when crossing the ionosphere. The ionosphere is an atmosphere layer consisting of free electrons and ions, which stretches from 50 to 1000 km altitude. The electric charges in this layer delay the propagation of the GNSS signal, affecting the code delay and phase measurements and introducing an error on the position estimation.

Fig. 2.8 illustrates the problem of determining the position from the GNSS observables. Each signal transverses a different path and therefore are expected to be affected by different ionospheric delays.

In this figure, the ionosphere is represented as a thin layer above the LEO heights. This representation, despite not being accurate, is in conformance with the widely used Lear ionosphere model [Lea87]. This model will also be used in this thesis. The ionospheric

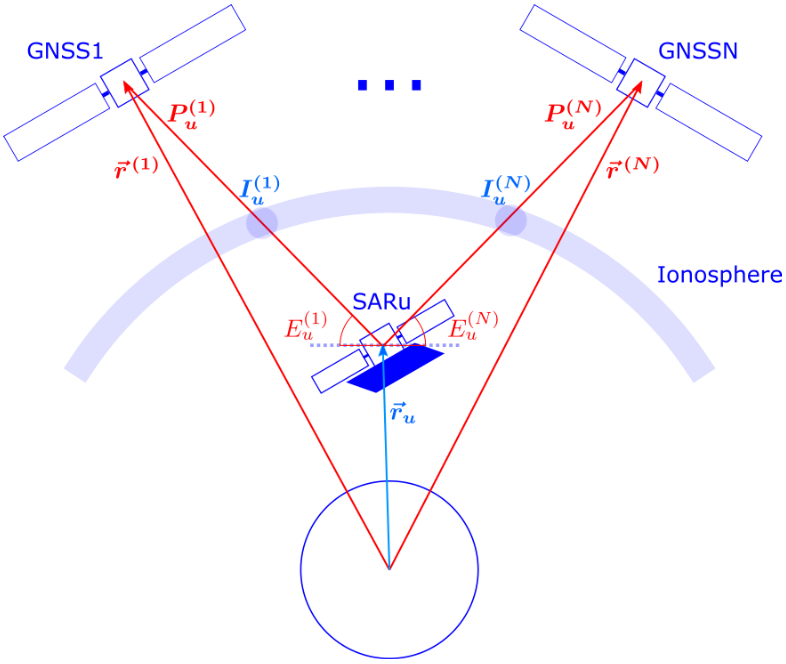

Figure 2.8: GNSS positioning principle.

delay ($I_u^{(i)}$) from satellite u to GNSS satellite i, in units of meters, is given by [HWC12]:

$$I_u^{(i)} = \frac{40.3\,[m^3/s^2]}{f^2}\mathrm{TEC}_u^{(i)}\,, \tag{2.9}$$

where c is the speed of light, f is the GNSS signal frequency, and TEC stands for the Total Electron Content expressed in the unit TECU ($1\,\mathrm{TECU} = 10^{16}\,el/m^2$), and computed by integrating the electron density ρ_{e^-} (number of electrons per unit of volume) along the signal path from the receiving satellite position (r_u) to the GNSS satellite position ($r^{(i)}$):

$$\mathrm{TEC}_u^{(i)} = \int_{r_u}^{r^{(i)}} \rho_{e^-} ds\,. \tag{2.10}$$

The factor 40.3 in Eq. (2.9) corresponds to the coefficient of the first term of a power series representation of the refraction index of the ionosphere [Klo95]. This equation covers only the first order ionospheric delay but offers sufficient precision, since ignoring higher order terms only result in errors on the sub-mm level [KH03]. The Lear model states that this equation can be approximated as a function of the elevation $E_u^{(i)}$ as follows:

$$\mathrm{TEC}_u^{(i)} = \frac{2.03}{\sin(E_u^{(i)}) + \sqrt{sin^2(E_u^{(i)}) + 0.076}} \mathrm{VTEC}_u \,. \tag{2.11}$$

In this equation, VTEC stands for Vertical Total Electron Content, which is a parameter given in TECU that does not depends on the specific viewing geometry, only on the satellite position.

The pseudorange measurements taking the ionospheric delay into consideration, for a receiver capable of receiving two frequencies f_1 and f_2 is given by

$$P_{u,1}^{(i)} = \rho_u^{(i)} + c\delta t_u + I_u^{(i)} + \epsilon_{uP,1}^{(i)} \,, \tag{2.12}$$

$$P_{u,2}^{(i)} = \rho_u^{(i)} + c\delta t_u + \left(\frac{f_1}{f_2}\right)^2 I_u^{(i)} + \epsilon_{uP,2}^{(i)} \,, \tag{2.13}$$

where $\rho_u^{(i)}$ is the distance from the receiver position vector $r_{uI} = [r_{uI} \quad r_{uJ} \quad r_{uK}]^T$ to the GNSS position vector $r^{(i)} = \left[r_I^{(i)} \quad r_J^{(i)} \quad r_K^{(i)}\right]^T$, given by

$$\rho_u^{(i)} = \sqrt{\left(r_{uI} - r_I^{(i)}\right)^2 + \left(r_{uJ} - r_J^{(i)}\right)^2 + \left(r_{uK} - r_K^{(i)}\right)^2} \,, \tag{2.14}$$

δt_u is the clock bias of the GNSS receiver with respect to the GPS time to which the GNSS satellites are synchronized and c is the speed of light in vacuum, $I_u^{(i)}$ is the total ionospheric delay for the signal at frequency f_1, and $\epsilon_{uP,2}^{(i)}$ and $\epsilon_{uP,2}^{(i)}$ are white Gaussian noise components.

The measured phase delays can be expressed as a ranging measurement in meters by multiplying it by the wavelength of the corresponding signal, which results in the phase-related range observables $L_{u,1}^{(i)}$ and $L_{u,2}^{(i)}$. These observables can be modeled as follows [Kro06]:

$$L_{u,1}^{(i)} = \rho_u^{(i)} + c\delta t_u - I_u^{(i)} + \lambda_1 A_{1u}^{(i)} + \epsilon_{uL,1}^{(i)} \,, \tag{2.15}$$

$$L_{u,2}^{(i)} = \rho_u^{(i)} + c\delta t_u - \left(\frac{f_1}{f_2}\right)^2 I_u^{(i)} + \lambda_2 A_{2u}^{(i)} + \epsilon_{uL,2}^{(i)} \,, \tag{2.16}$$

with A_{1u} and A_{2u} being the ambiguity terms explained earlier in this subsection, and $\epsilon_{uL,2}^{(i)}$ and $\epsilon_{uL,2}^{(i)}$ are white Gaussian noise components of the phase measurement. Note that the effect of the ionospheric delay in this case have the same magnitude but opposite signs compared to the code delay models. This is due to the fact that the ionosphere causes an advance on the phase and similarly a delay on the modulated code observation.

These equations give a model suitable for using in the position estimation algorithms with sufficient accuracy. For an arbitrary frequency k, the full error models are shown in equations includes an additional term

$$P_{u,k}^{(i)} = \rho_u^{(i)} + c\delta t_u + \left(\frac{f_1}{f_k}\right)^2 I_u^{(i)} + M_{uP}^{(i)} + \epsilon_{uP,k}^{(i)}\,, \tag{2.17}$$

$$L_{u,k}^{(i)} = \rho_u^{(i)} + c\delta t_u - \left(\frac{f_1}{f_k}\right)^2 I_u^{(i)} + \lambda A_{u,k}^{(i)} + M_{uL}^{(i)} + \epsilon_{uL,k}^{(i)}\,. \tag{2.18}$$

In these equations the additional term $M_{uP}^{(i)}$ and $M_{uL}^{(i)}$ encompass all additional errors and biases, including multipath effects, caused by the superposition of the signal received directly from the GNSS satellite and a signal reflected by the satellite surface, biases on the receiver channel, hardware delays on the GPS satellites and other systematic errors. These errors are further detailed in [Kro06]. We can always assume that the terms in $M_{uP}^{(i)}$ and $M_{uL}^{(i)}$ are calibrated from the data to a value below noise level, and thus can be considered as part of the noise component in equations (2.12) to (2.16).

In this thesis the models 2.12 and 2.13 are used for position estimation. For simplicity, the carrier phase will not be used because they demands special techniques for deducing the ambiguity, which are out of scope in this thesis.

2.2.3 Linearization for positioning

Because equation (2.14) is non linear with respect to the satellite position vector, the observable models given by the equations (2.12) to (2.16) are non linear with the respect to the parameters to be estimated. It is desirable to linearize the equations to allow us to employ the well consolidated and effective linear estimation techniques. Eq. (2.14) can be linearized around an initial estimate $\rho_{u0}^{(i)}$ as follows

$$\rho_u^{(i)} = \rho_{u0}^{(i)} - \vec{e}_u^{\,(i)} \cdot \Delta\vec{r}_u + \vec{e}_u^{\,(i)} \cdot \Delta\vec{r}^{\,(i)}\,, \tag{2.19}$$

in which the initial pseudorange estimate is defined as

$$\rho_{u0}^{(i)} = ||\vec{r}_{u0} - \vec{r}_0^{\,(i)}||\,, \tag{2.20}$$

and the initial unit vector between satellite and the i-th GNSS satellite $\vec{e}_u^{\,(i)}$ is defined as

$$\vec{e}_u^{\,(i)} = \frac{\vec{r}_{u0} - \vec{r}_0^{\,(i)}}{||\vec{r}_{u0} - \vec{r}_0^{\,(i)}||}\,. \tag{2.21}$$

This linearization is illustrated in Fig. 2.9. Replacing Eq. (2.19) in Eqs. (2.12) to (2.16) we obtain the final linearized equations for the carrier phase and code delay observables.

Defining the measurement errors as:

$$\Delta P_{1u}^{(i)} = P_{1u}^{(i)} - \rho_{u_0}^{(i)} - c\delta t_{u_0} - I_{u_0}^{(i)}\,, \tag{2.22}$$

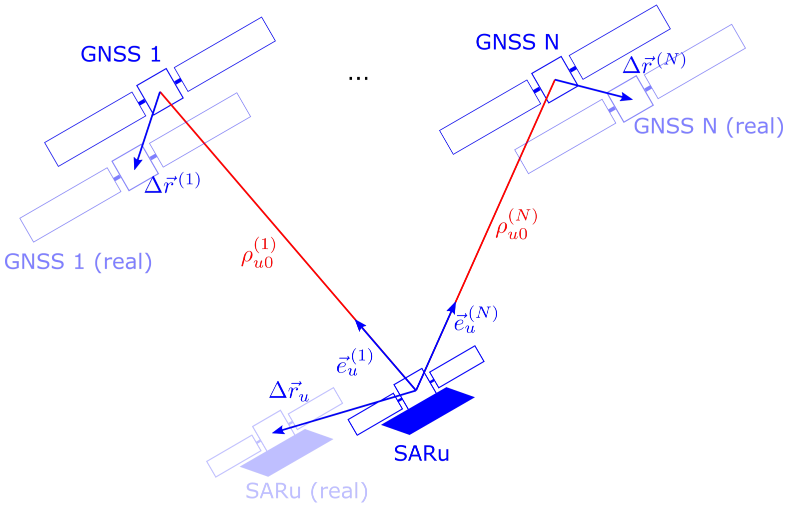

Figure 2.9: GNSS positioning linearization variables.

$$\Delta P_{2u}^{(i)} = P_{2u}^{(i)} - \rho_{u0}^{(i)} - c\delta t_{u0} - \left(\frac{f_1}{f_2}\right)^2 I_{u0}^{(i)}\,, \tag{2.23}$$

$$\Delta L_{1u}^{(i)} = L_{1u}^{(i)} - \rho_{u0}^{(i)} - c\delta t_{u0} - \lambda_1 A_{1u0}^{(i)} + I_{u0}^{(i)}\,, \tag{2.24}$$

$$\Delta L_{2u}^{(i)} = L_{2u}^{(i)} - \rho_{u0}^{(i)} - c\delta t_{u0} - \lambda_2 A_{2u0}^{(i)} + \left(\frac{f_1}{f_2}\right)^2 I_{u0}^{(i)}\,, \tag{2.25}$$

the final linearized equations for the carrier phase and code delay obseervables are given by:

$$\begin{aligned}\Delta P_{1u}^{(i)} = & -\frac{r_I^{(i)} - r_{u0I}}{\rho_{u0}^{(i)}}\Delta r_{uI} - \frac{r_J^{(i)} - r_{u0J}}{\rho_{u0}^{(i)}}\Delta r_{uJ} - \frac{r_K^{(i)} - r_{u0K}}{\rho_{u0}^{(i)}}\Delta r_{uK} + \\ & c\Delta\delta t_u + I_u^{(i)} + \epsilon_{uP,1}^{(i)}\,,\end{aligned} \tag{2.26}$$

$$\begin{aligned}\Delta P_{2u}^{(i)} = & -\frac{r_I^{(i)} - r_{u0I}}{\rho_{u0}^{(i)}}\Delta r_{uI} - \frac{r_J^{(i)} - r_{u0J}}{\rho_{u0}^{(i)}}\Delta r_{uJ} - \frac{r_K^{(i)} - r_{u0K}}{\rho_{u0}^{(i)}}\Delta r_{uK} + \\ & c\Delta\delta t_u + \left(\frac{f_1}{f_2}\right)^2 I_u^{(i)} + \epsilon_{uP,2}^{(i)}\,,\end{aligned} \tag{2.27}$$

$$\begin{aligned}\Delta L_{1u}^{(i)} = & -\frac{r_I^{(i)} - r_{u0I}}{\rho_{u0}^{(i)}}\Delta r_{uI} - \frac{r_J^{(i)} - r_{u0J}}{\rho_{u0}^{(i)}}\Delta r_{uJ} - \frac{r_K^{(i)} - r_{u0K}}{\rho_{u0}^{(i)}}\Delta r_{uK} + \\ & c\Delta\delta t_u - I_u^{(i)} + \lambda_1 A_{1u}^{(i)} + \epsilon_{uL,1}^{(i)}\,,\end{aligned} \tag{2.28}$$

$$
\begin{aligned}
\Delta L_{2u}^{(i)} = & -\frac{r_I^{(i)} - r_{u_0 I}}{\rho_{u_0}^{(i)}} \Delta r_{uI} - \frac{r_J^{(i)} - r_{u_0 J}}{\rho_{u_0}^{(i)}} \Delta r_{uJ} - \frac{r_K^{(i)} - r_{u_0 K}}{\rho_{u_0}^{(i)}} \Delta r_{uK} + \\
& c\Delta\delta t_u - \left(\frac{f_1}{f_2}\right)^2 I_u^{(i)} + \lambda_2 A_{2u}^{(i)} + \epsilon_{uL,2}^{(i)} \,.
\end{aligned}
\tag{2.29}
$$

2.2.4 Single difference model

When only relative positioning between two spacecrafts is required, one can use the difference between the observations taken at the receivers from both spacecrafts. By differentiating this data the common errors such as biases due to hardware delay are eliminated or greatly reduced. The ionospheric delay becomes very small, and can be reduced to sub-millimeter level if the satellites are at a distance of only a few kilometers.

2.2.5 Position estimation

2.2.5.1 Initial estimation

In order to apply an iterative linear estimator for the position we need an initial estimate of the position. An analytical solution is possible if we neglect the ionospheric delays. The equations below give a method for calculating the initial position from five pseudorange measurements from different satellites. These equations are derived by setting the ionospheric delay to zero in equation 2.12. This results in a system of four equations which allows for estimating the position vector and the clock bias. Five measurements are needed - instead of the minimum of four measurements for positioning - because the linear system of equations is obtained by subtracting the squared observables to eliminate the nonlinearities.

$$
\mathrm{A}_0 \cdot \begin{bmatrix} r_{uI} & r_{uJ} & r_{uK} & c\delta t_u \end{bmatrix}^T = \mathrm{B}_0 \,, \tag{2.30}
$$

with

$$
\mathrm{A}_0 = \begin{bmatrix}
2\left(r_I^{(1)} - r_I^{(2)}\right) & 2\left(r_J^{(1)} - r_J^{(2)}\right) & 2\left(r_K^{(1)} - r_K^{(2)}\right) & 2\left(P_u^{(2)} - P_u^{(1)}\right) \\
2\left(r_I^{(1)} - r_I^{(3)}\right) & 2\left(r_J^{(1)} - r_J^{(2)}\right) & 2\left(r_K^{(1)} - r_K^{(3)}\right) & 2\left(P_u^{(3)} - P_u^{(1)}\right) \\
2\left(r_I^{(1)} - r_I^{(4)}\right) & 2\left(r_J^{(1)} - r_J^{(2)}\right) & 2\left(r_K^{(1)} - r_K^{(4)}\right) & 2\left(P_u^{(4)} - P_u^{(1)}\right) \\
2\left(r_I^{(1)} - r_I^{(5)}\right) & 2\left(r_J^{(1)} - r_J^{(2)}\right) & 2\left(r_K^{(1)} - r_K^{(5)}\right) & 2\left(P_u^{(5)} - P_u^{(1)}\right)
\end{bmatrix} , \tag{2.31}
$$

and

$$\mathrm{B}_0 = \begin{bmatrix} -\left\|\vec{r}^{(2)}\right\|^2 + \left\|\vec{r}^{(1)}\right\|^2 + \left(P_u^{(2)}\right)^2 - \left(P_u^{(1)}\right)^2 \\ -\left\|\vec{r}^{(3)}\right\|^2 + \left\|\vec{r}^{(1)}\right\|^2 + \left(P_u^{(3)}\right)^2 - \left(P_u^{(1)}\right)^2 \\ -\left\|\vec{r}^{(4)}\right\|^2 + \left\|\vec{r}^{(1)}\right\|^2 + \left(P_u^{(4)}\right)^2 - \left(P_u^{(1)}\right)^2 \\ -\left\|\vec{r}^{(5)}\right\|^2 + \left\|\vec{r}^{(1)}\right\|^2 + \left(P_u^{(5)}\right)^2 - \left(P_u^{(1)}\right)^2 \end{bmatrix} . \tag{2.32}$$

This initial position estimation was used thorough the several cases tested in this thesis and it has always presented good results. This estimate yielded errors from 10 to 30 meters in the test scenarios, which is very small compared to the absolute values fo the position vector.

2.2.5.2 Linearized weighted least-squares estimation

Defining a state matrix X and a measurement matrix Y, assume the measurements are a stochastic process defined as a function h of the states plus a noise process described by the gaussian vector ϵ of covariance matrix $\mathrm{cov}(\epsilon, \epsilon) = Q$. In this case the measurements are given by the equation:

$$\mathrm{Y} = h(\mathrm{X}) + \epsilon \, . \tag{2.33}$$

Assume an initial estimate X_0 of the state matrix is known. Defining the matrices:

$$\mathrm{A} = \left. \frac{\partial h(\mathrm{X})}{\partial \mathrm{X}} \right|_{\mathrm{X}=\mathrm{X}_0} , \tag{2.34}$$

$$\Delta\mathrm{X} = \mathrm{X} - \mathrm{X}_0 \, , \tag{2.35}$$

$$\Delta\mathrm{Y} = \mathrm{Y} - h(\mathrm{X}) \, , \tag{2.36}$$

if X_0 is sufficiently close to X, Eq. (2.33) can be approximated as follows:

$$\Delta\mathrm{Y} = \mathrm{A} \cdot \Delta\mathrm{X} + \epsilon \, . \tag{2.37}$$

Given the set of measurements Y, we want to find a correction vector $\Delta\mathrm{X}_{LS}$ such that the resulting measurement error vector $\Delta\mathrm{Y}$ is minimized in the least square sense, or:

$$\Delta\mathrm{X}_{LS} = \arg\min_{\Delta\mathrm{X}} ||\mathrm{Y} - h(\mathrm{X} + \Delta\mathrm{X})||^2 \, . \tag{2.38}$$

The covariance of this estimate is given by

$$\left(\mathrm{A}^T \mathrm{Q}^{-1} \mathrm{A}\right) \Delta\mathrm{X} = \mathrm{A}^T \mathrm{Q}^{-1} \Delta\mathrm{Y} \, . \tag{2.39}$$

The covariance of this estimate is given by

$$\mathrm{P}_{xx} = \left(\mathrm{A}^T \mathrm{Q}^{-1} \mathrm{A}\right)^{-1} . \tag{2.40}$$

Finally, the corrected state vector is given by

$$\mathrm{X} = \mathrm{X}_0 + \Delta\mathrm{X} . \tag{2.41}$$

The algorithm described here is based on the solution of determining an optimal estimate of a state from measurements which are a linear function of the state plus an additive white Gaussian noise. Since the system is non-linear, this is an approximation and the algorithm must be run iteratively to reach an optimal solution. At each iteration X_0 is replaced by X estimated at the previous step, until a stop criterion is fulfilled. This stop criterion can be, for example, if the norm of $\Delta\mathrm{X}$ is below a minimum threshold.

For simplest GNSS position estimation, using only code delay measurements and for a receiver able to receive two frequencies, the states are the position components, the clock bias and the ionospheric delays, one for each GNSS signal tracked, and the measurements are described by the equations 2.12 and 2.13. If N is the number of GNSS satellites being tracked at a given instant, the number of measurements in this case would be $2N$, and the number of estimated variables would be $4 + N$, comprising the position components, the clock bias and the N ionospheric delays.

2.2.6 Precise orbit and baseline determination

The algorithm described previously corresponds to a purely kinematic position estimation algorithm, which has the advantage of requiring no a-priori knowledge of the spacecraft motion. This solution achieves several to tens of meters and suffices for many navigation applications. A kinematic GNSS based Precise Orbit Determination is possible by processing a data set containing code delay and carrier phase information for a long time period in a single batch least-squares estimator. By using measurements from different time steps, it is possible to solve for the ambiguities, since they remain constant for a tracking period. By solving for the ambiguities it is possible to use the more precise carrier phase measurements in the estimation, which yield better results compared to a solution based on the data from a single time step using only code delay data. This, however, demands the use of special numerical techniques to deal with the long systems of equation, comprising possibly thousands of equations [Kro06].

By using information about the expected dynamic behavior of the spacecraft orbit given an initial state, the estimation can be greatly improved. These algorithms, however, involve an extremely detailed model of the orbital dynamics, including a model of the gravity field of high degree, the effects of polar tides and ocean tides, Sun and Moon attraction, relativistic effects, atmospheric drag, solar radiation pressure, etc. Techniques based on dynamic models allows for a very precise orbit determination, in the order of centimeters for absolute positioning and below millimeter in relative positioning. The dynamic solutions can be approached also using batch least-squares or extended Kalman filters.

Chapter 3 focuses on applying the purely point by point kinematic position estimation based on the background given in this chapter. The objective is to have comparative position estimation results for several different cases involving different numbers of satellites, geometry and additional information provided by other hardware. The comparative results will give information on the information content of each configuration hinting the possibility of improvement when applying the final algorithm for precise orbit determination.

In chapter 4, which is focused on phase estimation and not on positioning, we assume the input orbital data to be in line with the state-of-the-art Precise Orbit Determination in terms of precision.

2.3 Reference frames

This section defines the frames used through the thesis to express the input trajectory data and the positioning results. The orbital data is expressed in an Earth-Centered Inertial Frame. This frame is centered on Earth and fixed with respect to the stars. It is defined as having the mean equinox as the x direction and the equatorial plane as the reference plane. There are different realizations of this frame, the one used in this work was the J2000 frame, defined from the Earth's Mean Equator and Equinox at 12:00 Terrestrial Time on 1 January 2000.

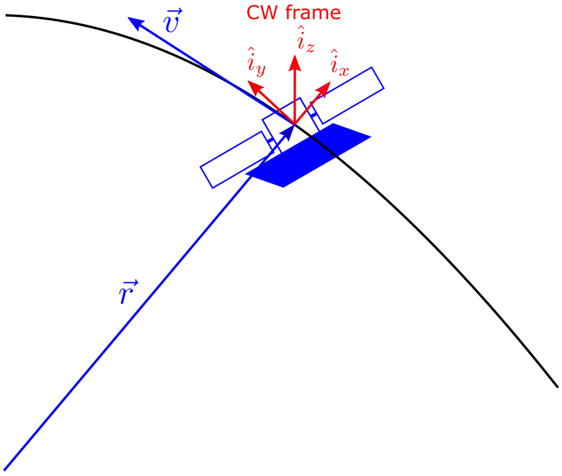

Figure 2.10: Clohessy-Wiltshire frame definition.

The three unit vectors forming the CW frame are defined from the spacecraft position ($\vec{r}$) and velocity vector ($\vec{v}$) as follows:

$$\hat{i}_x = \frac{\vec{r}}{||\vec{r}||}\,, \tag{2.42}$$

$$\hat{i}_z = \frac{\vec{r} \times \vec{v}}{||\vec{r} \times \vec{v}||}\,, \tag{2.43}$$

$$\hat{i}_y = \frac{\hat{i}_z \times \hat{i}_x}{||\hat{i}_z \times \hat{i}_x||}\,. \tag{2.44}$$

The components x, y and z of a vector in the CW frame will be referred to in this thesis as radial, along-track and across-track, respectively. These components provide a better insight on the problem since they are more directly associated with the viewing geometry between the LEO satellites and the GNSS constellation.

The CW frame has to be calculated from the orbital data in ECI frame at each time step, and from the unit vectors defining the CW frame one can calculate the coordinates transformation matrix. Given that the unit vectors $\hat{i}_x$, $\hat{i}_y$ and $\hat{i}_z$ expressed in ECI frame, the transformation matrix from ECI to CW frame ${}^{i}\mathrm{T}_{cw}$ is given by

$${}^{i}\mathrm{T}_{cw} = \begin{bmatrix} \hat{i}_x & \hat{i}_y & \hat{i}_z \end{bmatrix}\,. \tag{2.45}$$

Besides allowing for more insight in the results, the CW frame greatly simplifies the description of the relative movement between two satellites flying in close distance. The so-called Clohessy-Wiltshire equations describe the relative motion of two satellites with almost identical, near-circular orbits. It reveals that the one satellite describes an elliptical motion around the other under certain circumstances. The formations used as test cases in this thesis are calculated based on solutions for the Clohessy-Wiltshire equations. For this thesis it is sufficient to describe the final relative motion of the spacecrafts, which will be considered as an input, and the details on how those orbits were calculated are left out of the scope of this thesis. For more details on spacecraft relative motion refer to [Val01].

3 Multisatellite Position Determination

This chapter presents a study on position determination of satellites flying in formation, using GNSS data combined with information derived from other embedded hardware. The position determination algorithms are formulated such that the data from all the satellites in the formation is processed coherently in a single batch least squares estimator. A simulated environment was developed to generate all the data necessary for testing the algorithms. The accuracies attained by each of the position determination algorithms, for different numbers of satellites, are compared. The result gives an insight on the information content of each data combination, and allows us to draw conclusions on the possibility of exploiting them in more sophisticated Precise Orbit Determination (POD) algorithms for more accurate position and baseline estimates.

The first section in this chapter details the algorithms and their underlying assumptions. The second section explains the simulation framework. Finally, the third section presents the results from the simulations and conclusions drawn from them.

3.1 Algorithms descriptions

Four different scenarios are presented in this section. In all scenarios the satellites are assumed to be flying close enough to each other, at distances of less than one kilometer, so that the ionospheric delays affecting the signals received in the satellites are highly correlated. For simplicity, every algorithm uses data from a single time step and only code-delay information. The carrier phase information, although included in the simulation framework, is not used in order to avoid rank deficiency problems in the design matrix due to the addition of the ambiguity terms in the estimation parameters. In all scenarios the measurements obtained from one satellite relates to at least one estimation parameter related to other satellites, which justifies the coherent processing of the data.

In the first scenario we assume that every satellite is equipped only with dual frequency GNSS receivers. In this case, the common estimation parameter is the highly correlated ionospheric delay between satellites. This is the base scenario, upon which the other scenarios are built.

In the second scenario, one satellite is provided with a dual frequency receiver and all the others with a single frequency receivers. The common parameter in this case is also the highly correlated ionospheric delay between satellites in close formation. The advantage of this constellation architecture is that we can use the capability of estimating the ionospheric delay from the dual frequency receiver to improve the estimation results for the other satellites.

The third scenario consists in adding to the base scenario an inter-satellite ranging system providing an unbiased measurement of the distance between two of the satellites in the formation. This additional information is expected to improve the baseline and position estimates compared to the first and second case. The improvement in this case is expected to be particularly dependent on the relative geometry of the satellites, since this geometry determines to which degree the scalar distance measurement offers information on each component of the baseline. This tests aims also at determining whether there is an improvement on the baseline between one satellite with inter-satellite ranging and one without it.

The fourth and last scenario consists in using information on the baseline provided by interferometric data, and is specific for multistatic SAR applications. In interferometry, the elevation of the scenery is retrieved by combining the images from two satellites. The resulting Digital Elevation Model (DEM) relies on very precise baseline determination. An error in the baseline translates into an error in the calculated elevations. A digital elevation model is built using data from two SAR satellites, and an error in the baseline between these two satellites will introduce a bias in the elevation profile. Two different pairs of satellites imaging the same region should, in an ideal case, generate very similar DEMs. A difference in the baselines errors would cause a bias between the synthesized DEMs, which can be formulated as a function of those errors. Therefore, this bias consists in an indirect measurement of the baselines. The solution proposed in this scenario consists in using this bias in a estimator, along with data from the dual frequency receivers.

All the estimation algorithms are Linear Least Square estimators, as described in section 2.2.5. For each estimator, four components are needed to describe the problem: the states correction matrix (ΔX), the measurements error matrix (ΔY), the design matrix (A) and the measurements covariance matrix (Q). The following subsections detail the algorithms and define each of those components for each scenario.

In each estimator, the position, clock bias and ionospheric delays are calculated. The baselines are calculated by subtracting the estimated position vector between two satellites. Note that by using differenced GNSS data, one could formulate the estimation problem in terms of the baseline vector instead of the individual position vectors, as is done here. In this approach, it is easy to see that the ionospheric delays cancel out by taking the single difference, which explains the sensibly better baseline accuracy attained compared to absolute position estimations. Although not obvious at first glance, the two approaches - calculating baseline from coherently estimated position vectors and estimating the baselines directly from differenced data - yield almost identical results, with divergences on the order of tenths of millimeter. The reason is that processing the position vectors coherently results in correlated errors in the positions which cancel out when subtracting them. This equivalence of the two methods was demonstrated in preliminary tests to decide in which approach to follow. In the end, the approach based on absolute position was chosen because is also offers insight into the position determination problem.

3.1.1 Multi-satellite with dual frequency receivers

Fig. 3.1 illustrates the problem of position determination for three satellites using code delay measurements. The measurements are shown in red and the estimated parameters in blue. The ionosphere is illustrated as a thin layer between MEO and LEO, which is in accordance with the LEAR model for the ionospheric delay used thorough the thesis. Note that this is just a representation. As mentioned in 2, the ionosphere is a continuous layer which extends from roughly 50 km to 1000 km altitude. The figure shows three satellites, but the equations derived in this section are for a generic number of n LEO satellites and N visible GNSS satellites.

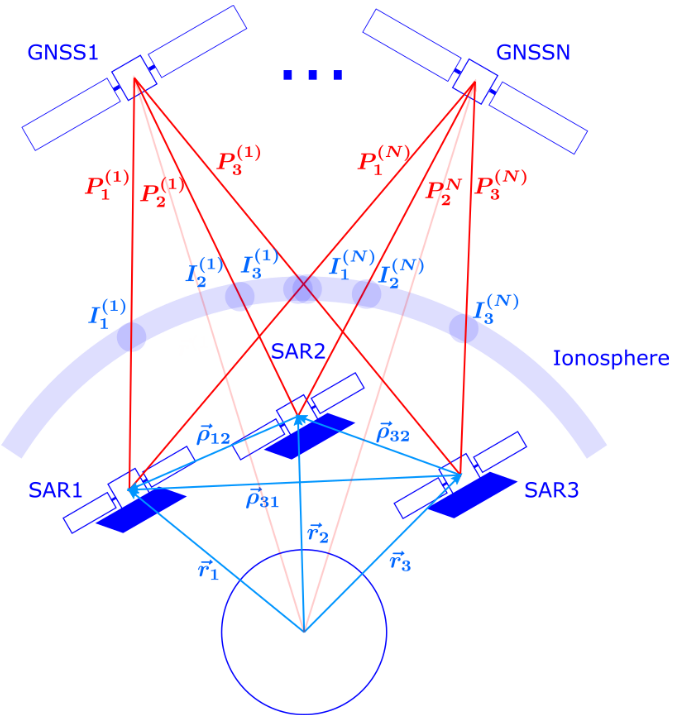

Figure 3.1: Multi-satellite positioning.

The variables to be estimated are the position vector, the clock biases and the ionospheric delays for each satellite. Given an initial estimate of each state, for each satellite we can define a sub-state correction vector ($\Delta \mathrm{X}_u$) as follows

$$\Delta \mathrm{X}_u = \begin{bmatrix} \Delta r_{uI} & \Delta r_{uJ} & \Delta r_{uK} & \Delta \delta t_u \end{bmatrix}^T . \tag{3.1}$$

Assuming that the satellites fly at a distance of no more than one kilometer from each other, the LEAR model for the ionospheric delay given by equation 2.9 predicts that the ionospheric delay affecting the signal received from the same GNSS satellite will be approximately the same for every satellite in the formation, which is expressed in Eq.

(3.2) below:

$$\Delta I_1^{(i)} = \Delta I_2^{(i)} = \cdots = \Delta I_n^{(i)} \,. \tag{3.2}$$

This assumption greatly reduces the number of ionospheric delays to be estimated. Defining the ionospheric delay correction vector as

$$\Delta \mathrm{I} = \begin{bmatrix} \Delta I^{(1)} & \Delta I^{(1)} & \cdots & \Delta I^{(N)} \end{bmatrix}^T \,, \tag{3.3}$$

we can define the full state correction vector as

$$\Delta \mathrm{X} = \begin{bmatrix} (\Delta \mathrm{X}_1)^T & \cdots & (\Delta \mathrm{X}_n)^T & \Delta \mathrm{I}^T \end{bmatrix}^T \,. \tag{3.4}$$

Based on the linearized GNSS observation model, given by Eqs. 2.26 to 2.27, we can define a measurement error vector ($\Delta \mathrm{Y}_{u,1}$) for a given spacecraft u and for the reference frequency, with respect to which the ionospheric delays $\Delta I^{(N)}$ are defined, as

$$\Delta \mathrm{Y}_{u,1} = \begin{bmatrix} P_{u,1}^{(1)} - \rho_{u_0}^{(1)} - c\delta t_{u_0} - I_{u_0}^{(1)} \\ P_{u,1}^{(2)} - \rho_{u_0}^{(2)} - c\delta t_{u_0} - I_{u_0}^{(2)} \\ \vdots \\ P_{u,1}^{n} - \rho_{u_0}^{n} - c\delta t_{u_0} - I_{u_0}^{n} \end{bmatrix} \,, \tag{3.5}$$

and the for second frequency as

$$\Delta \mathrm{Y}_{u,2} = \begin{bmatrix} P_{u,2}^{(1)} - \rho_{u_0}^{(1)} - c\delta t_{u_0} - \left(\frac{f_1}{f_2}\right)^2 I_{u_0}^{(1)} \\ P_{u,2}^{(2)} - \rho_{u_0}^{(2)} - c\delta t_{u_0} - \left(\frac{f_1}{f_2}\right)^2 I_{u_0}^{(2)} \\ \vdots \\ P_{u,2}^{n} - \rho_{u_0}^{n} - c\delta t_{u_0} - \left(\frac{f_1}{f_2}\right)^2 I_{u_0}^{n} \end{bmatrix} \,. \tag{3.6}$$

The full measurement error vector is a combination of all the measurements errors for every frequency and spacecraft. It can be defined as in Eq. (3.7) below

$$\Delta \mathrm{Y} = \begin{bmatrix} (\Delta \mathrm{Y}_{1,1})^T & \cdots & (\Delta \mathrm{Y}_{n,1})^T & (\Delta \mathrm{Y}_{1,2})^T & \cdots & (\Delta \mathrm{Y}_{n,2})^T \end{bmatrix}^T \,. \tag{3.7}$$

Having defined the state correction vector $\Delta \mathrm{X}$ and the full measurement error vector $\Delta \mathrm{Y}$, the design matrix A is uniquely defined from Eqs. 2.26 and 2.27. Defining the terms

$$e_{uI}^{(i)} := \frac{r_I^{(i)} - r_{u_0 I}}{\rho_{u_0}^{(i)}} \,, \tag{3.8}$$

$$e_{uJ}^{(i)} := \frac{r_J^{(i)} - r_{u_0 J}}{\rho_{u_0}^{(i)}} \,, \tag{3.9}$$

$$e_{uK}^{(i)} := \frac{r_K^{(i)} - r_{u_0 K}}{\rho_{u_0}^{(i)}}, \tag{3.10}$$

for each satellite u, the state correction $\Delta \mathrm{X}_u$ relates to the measurement $\Delta \mathrm{Y}_{u,1}$ and $\Delta \mathrm{Y}_{u,2}$ through the following sub-matrix:

$$\mathrm{E}_u = \begin{bmatrix} -e_{uI}^{(1)} & -e_{uJ}^{(1)} & -e_{uK}^{(1)} & 1 \\ -e_{uI}^{(2)} & -e_{uJ}^{(2)} & -e_{uK}^{(2)} & 1 \\ \vdots & \vdots & \vdots & \vdots \\ -e_{uI}^{(n)} & -e_{uJ}^{(n)} & -e_{uK}^{(n)} & 1 \end{bmatrix}. \tag{3.11}$$

Each state correction $\Delta \mathrm{X}_u$ is dependent only on the measurements coming from the receiver in the satellite u. The only common factor which is affected by measurements across satellites is the ionospheric delay, under the assumption stated in Eq. (3.2). The final design matrix A is given by

$$\mathrm{A} = \begin{bmatrix} \mathrm{E}_1 & \mathbb{0}_{N,4} & \cdots & \mathbb{0}_{N,4} & \mathbb{1}_{N,N} \\ \mathbb{0}_{N,4} & \mathrm{E}_2 & \cdots & \mathbb{0}_{N,4} & \mathbb{1}_{N,N} \\ \vdots & \vdots & \ddots & \vdots & \vdots \\ \mathbb{0}_{N,4} & \mathbb{0}_{N,4} & \cdots & \mathrm{E}_n & \mathbb{1}_{N,N} \\ \mathrm{E}_1 & \mathbb{0}_{N,4} & \cdots & \mathbb{0}_{N,4} & \left(\frac{f_1}{f_2}\right)^2 \cdot \mathbb{1}_{N,N} \\ \mathbb{0}_{N,4} & \mathrm{E}_2 & \cdots & \mathbb{0}_{N,4} & \left(\frac{f_1}{f_2}\right)^2 \cdot \mathbb{1}_{N,N} \\ \vdots & \vdots & \ddots & \vdots & \vdots \\ \mathbb{0}_{N,4} & \mathbb{0}_{N,4} & \cdots & \mathrm{E}_n & \left(\frac{f_1}{f_2}\right)^2 \cdot \mathbb{1}_{N,N} \end{bmatrix}, \tag{3.12}$$

where $\mathbb{0}_{x,y}$ denotes a null matrix of x lines and y columns, and $\mathbb{1}_{N,N}$ denotes the identity matrix of dimensions N. As shown in Eq. (3.12), each satellite adds more information on each ionospheric delay term, as long as the assumption expressed in Eq. (3.2) is true. Therefore, it is expected that each added satellite improves the ionospheric delay estimate accuracy, and by consequence also the position and clock bias estimates.

Finally, the covariance matrix for the measurements has to be defined. All the measurements can be assumed to be independent from each other. For simplicity, we can assume that every measurement have the same standard deviation (σ_P), which results in the following covariance matrix:

$$\mathrm{Q} = \sigma_P \cdot \mathbb{1}_{2N \cdot n, 2N \cdot n} \tag{3.13}$$

In a real scenario the covariance of each measurement will differ, specially due to the difference in viewing geometries for signals coming from different GNSS satellites and this would have to be taken into account in the matrix Q. However, this is not expected to affect the comparative results and thus is not included in the simulations.

3.1.2 One satellite with double frequency, the others with single frequency receivers

The second test case is illustrated in Fig. 3.2. In this case, one satellite is equipped with a dual-frequency receiver, illustrated in blue, and the remaining satellites are equipped with single-frequency receivers, indicated in red.

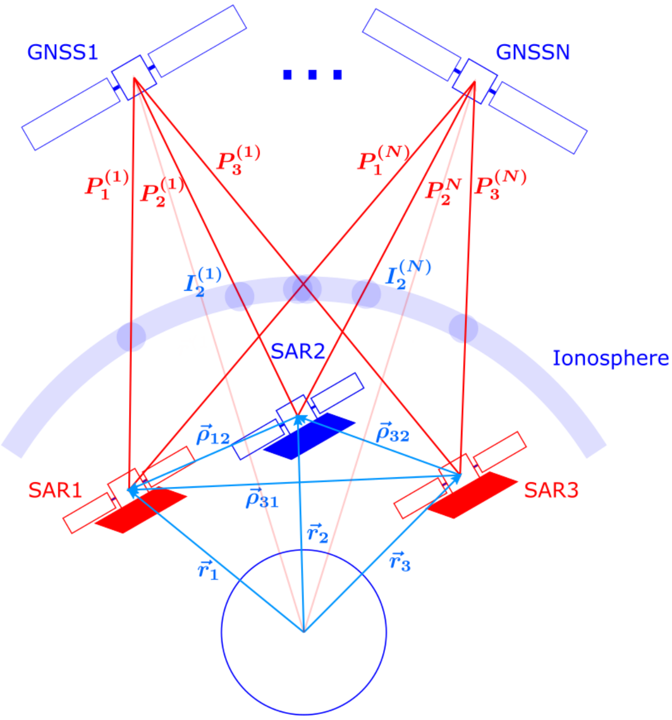

Figure 3.2: Multi-satellite positioning with receivers of different capabilities.

The states remain the same as in the first case, and is given by Eq. (3.4), but now we have measurements on the second frequency only on a single satellite. The measurement correction vector in this case can be defined as

$$\Delta \mathrm{Y} = \left[(\Delta \mathrm{Y}_{1,1})^T \quad (\Delta \mathrm{Y}_{2,1})^T \quad \cdots \quad (\Delta \mathrm{Y}_{n,1})^T \quad (\Delta \mathrm{Y}_{1,2})^T \right]^T , \tag{3.14}$$

where $\Delta \mathrm{Y}_{u,1}$ and $\Delta \mathrm{Y}_{u,2}$ are defined by Eqs. (3.5) and (3.6). The design matrix in this case is given by

$$\mathrm{A} = \begin{bmatrix} \mathrm{E}_1 & \mathbb{0}_{N,4} & \cdots & \mathbb{0}_{N,4} & \mathbb{1}_{N,N} \\ \mathbb{0}_{N,4} & \mathrm{E}_2 & \cdots & \mathbb{0}_{N,4} & \mathbb{1}_{N,N} \\ \vdots & \vdots & \ddots & \vdots & \vdots \\ \mathbb{0}_{N,4} & \mathbb{0}_{N,4} & \cdots & \mathrm{E}_n & \mathbb{1}_{N,N} \\ \mathrm{E}_1 & \mathbb{0}_{N,4} & \cdots & \mathbb{0}_{N,4} & \left(\frac{f_1}{f_2}\right)^2 \mathbb{1}_{N,N} \end{bmatrix} , \tag{3.15}$$

and the covariance matrix by

$$\mathrm{Q} = \sigma_P \cdot \mathbb{1}_{N\cdot(n+1),N\cdot(n+1)} \,. \tag{3.16}$$

Note that since only one spacecraft is able to calculate the common parameter which is the ionospheric delay, neither the baseline nor the position accuracy are expected to improve with the number of satellites. However, the satellites with less capable receivers may benefit from the ionosphere estimation made possible by the satellite with dual frequency receiver.

3.1.3 Multi-satellite with dual frequency receivers and inter-satellite ranging between two satellites

The third test case is illustrated in Fig. 3.3. In this case a direct measurement of the distance between two satellites through an inter-satellite ranging system is added.

The inter-satellite ranging can be modelled as the physical distance between the satellites plus a noise component as follows

$$R_{uv} = \sqrt{(r_{vI} - r_{uI})^2 + (r_{vJ} - r_{uJ})^2 + (r_{vK} - r_{uK})^2} + \epsilon_{\mathrm{rng}} \,. \tag{3.17}$$

This is a non-linear equation in terms of the estimation variables, so we need to linearize it around an initial estimates for the position vectors, here denoted $\vec{r}_{u0} = [r_{uI0} \quad r_{uJ0} \quad r_{uK0}]^T$ and $\vec{r}_{v0} = [r_{vI0} \quad r_{vJ0} \quad r_{vK0}]^T$. Defining

$$R_{uv0} = \sqrt{(r_{vI0} - r_{uI0})^2 + (r_{vJ0} - r_{uJ0})^2 + (r_{vK0} - r_{uK0})^2} \,, \tag{3.18}$$

the inter-satellite ranging measurement error is defined as

$$\Delta R_{uv} = R_{uv} - R_{uv_0} \,. \tag{3.19}$$

Linearizing Eq. (3.17) around an initial estimate, we have

$$\begin{aligned} \Delta R_{uv} \approx & - \frac{(r_{vI_0} - r_{uI_0})}{R_{uv_0}} \Delta r_{uI} - \frac{(r_{vJ_0} - r_{uJ_0})}{R_{uv_0}} \Delta r_{uJ} - \frac{(r_{vK_0} - r_{uK_0})}{R_{uv_0}} \Delta r_{uK} + \\ & \frac{(r_{vI_0} - r_{uI_0})}{R_{uv_0}} \Delta r_{vI} + \frac{(r_{vJ_0} - r_{uJ_0})}{R_{uv_0}} \Delta r_{vJ} + \frac{(r_{vK_0} - r_{uK_0})}{R_{uv_0}} \Delta r_{vK} + \epsilon_{\mathrm{rng}} \end{aligned} \,. \tag{3.20}$$

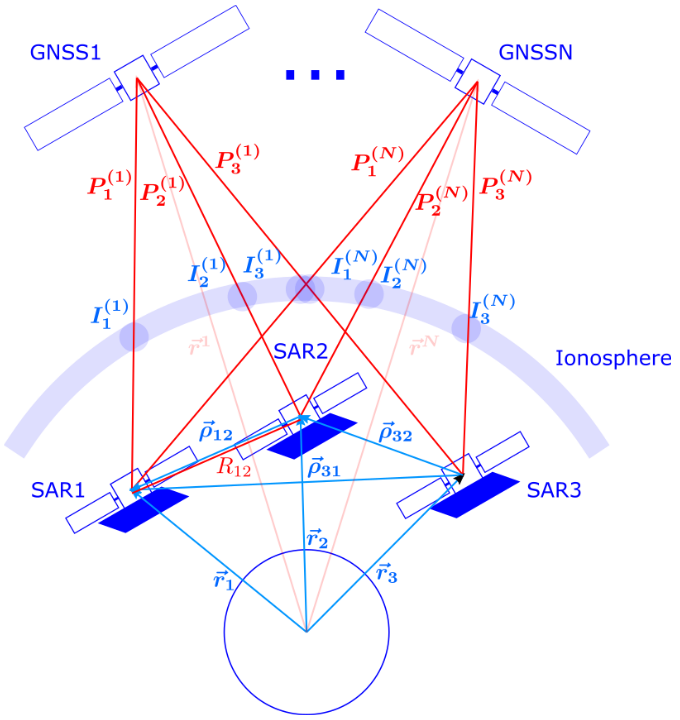

Figure 3.3: Multi-satellite positioning with inter-satellite ranging information.

Defining the term

$$\mathrm{E}_{uv} = \begin{bmatrix} \frac{\left(r_{vI_0} - r_{uI_0}\right)}{R_{uv_0}} & \frac{\left(r_{vJ_0} - r_{uJ_0}\right)}{R_{uv_0}} & \frac{\left(r_{vK_0} - r_{uK_0}\right)}{R_{uv_0}} & 0 \end{bmatrix} , \tag{3.21}$$

the line of the design matrix corresponding to the intersatellite range between u and v is given by

$$\mathrm{A}_{Ruv} = \begin{bmatrix} \mathbb{0}_{1,4(u-1)} & -\mathrm{E}_{uv} & \mathbb{0}_{1,4(v-u-1)} & \mathrm{E}_{uv} & \mathbb{0}_{1,4(n-v)+N} \end{bmatrix} . \tag{3.22}$$

The layout of the full matrix depends on the specific satellites in the constellation which share an intersatellite ranging system. The final estimator will be obtained by appending the ranging measurements to the measurement error matrix $\Delta\mathrm{Y}$ and the matrices A_{Ruv} to the the design matrix in Eqs. (3.7) and (3.12) of the base scenario.

Given that the inter-satellite ranging is uncorrelated with the other measurements, and denoting the standard deviation of its noise process ϵ_{rng} as σ_{rng}, and the total number of intersatellite ranges available at a instant in time as n_{rng}, the total covariance matrix is given by

$$\mathrm{Q} = \begin{bmatrix} \sigma_P \cdot \mathbb{1}_{2N,2N} & \mathbb{0}_{2N,n_{\mathrm{rng}}} \\ \mathbb{0}_{n_{\mathrm{rng}},2N} & \sigma_{\mathrm{rng}} \cdot \mathbb{1}_{n_{\mathrm{rng}},n_{\mathrm{rng}}} \end{bmatrix} . \tag{3.23}$$

In this case it is clear that the additional equation provides a new independent measurement on the positions and baselines. This test scenario will determine to which extent this will improve the baseline, and if the orbit geometry will have an influence on this improvement.

3.1.4 Multi-satellite with dual frequency receivers and interferometric data

The last scenario evaluates the possibility of using interferometric data to improve the baseline estimation, it is illustrated in Fig. 3.4. In the example shown in the figure, three SAR spacecrafts collect SAR data from the same area. From each pair of satellites a Digital Elevation Model (DEM) of the area can be synthesized. The figure represents a projection in the plane orthogonal to the chief satellite velocity vector.

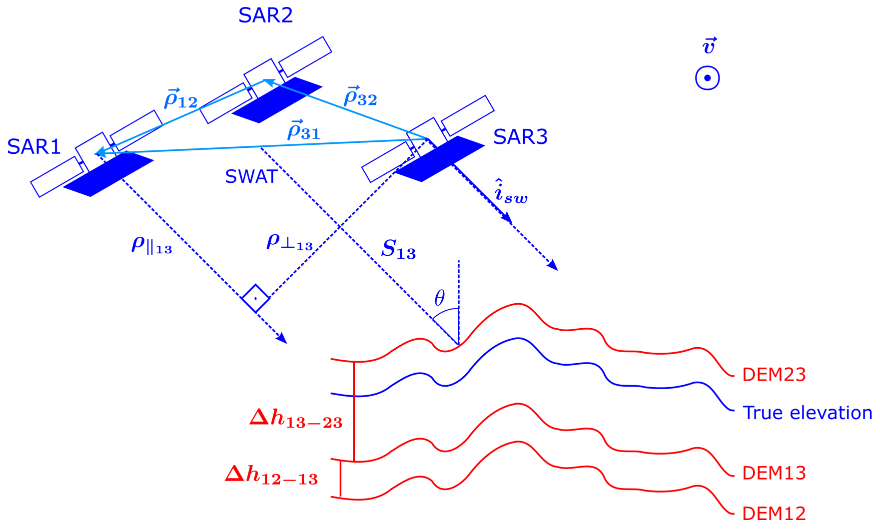

Figure 3.4: Baseline error effect on DEM height offset.

A precise estimate of the baseline between the satellites is needed to synthesize the DEM. An error in the baseline components parallel and orthogonal to the line-of-sight direction vector ($\hat{i}_{SW}$) will result into an height bias on the DEM. Denoting $\Delta\rho_{\|_{uv}}$ the baseline error component parallel to the line of sight direction vector and $\rho_{\perp_{uv}}$ the baseline component orthogonal to the line-of-sight direction vector and to the velocity vector, the error in the height of the calculated DEM due to the parallel component of the baseline error is given by the following equation [KMF$^+$07]:

$$\Delta h_{uv} = \frac{S_{uv}\sin(\theta)}{\rho_{\perp_{uv}}} \cdot \Delta\rho_{\|_{uv}}\,, \tag{3.24}$$

where θ and S_{uv} are the incident angle and the slant range of an appropriately selected reference point, in this case the midswath, as illustrated in Fig. 3.4. As discussed in [KMF$^+$07], the height offset due to the parallel baseline error component is approximately two order of magnitude greater than the height offset due to an error in the orthogonal baseline component. Therefore, in this analysis only the parallel component of the height error will be considered.

In the case illustrated in Fig. 3.4, three possible combinations of satellites result in three DEMs with the same shape but different height offsets, since each combination will result in a different baseline error. It is not possible to directly measure the true elevation from the data, but the fact that the mismatch between DEMs have a direct relationship with the baseline errors can be exploited. The proposed estimation algorithm using the DEM information is shown in Fig. 3.5. The baseline is initially determined using the GNSS data, which allows us to synthesize DEMs from the SAR data. By comparing the DEMs we can derive height offsets, which are used to refine the baseline estimation. The algorithm is run interactively until the baselines converge.

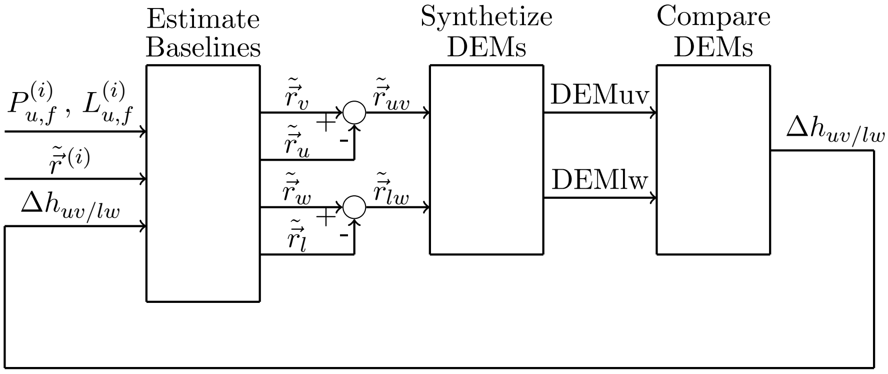

Figure 3.5: Proposed DEM-based baseline calibration scheme.

In order to implement the estimator shown in Fig. 3.5, we need a linearized description of the relation between the measurements ($\Delta h_{uv/lw}$) and the states. Consider a constellation of n SAR satellites imaging the same area and the DEMs formed by two arbitrary pairs of satellite in this constellation, one from satellites u and v and one from satellites l and w. The observed height offset between the two DEMs ($\Delta h_{uv/lw}$) can be modelled from Eq. (3.24) as follows

$$\Delta h_{uv/lw} = \frac{S_{lw}\sin(\theta)}{\rho_{\perp_{lw}}} \cdot \Delta\rho_{\|_{lw}} - \frac{S_{uv}\sin(\theta)}{\rho_{\perp_{uv}}} \cdot \Delta\rho_{\|_{uv}} + \epsilon_{DEM} \,, \tag{3.25}$$

where ϵ_{DEM} is a zero mean Gaussian process of standard deviation σ_{DEM} which models the various error sources in the SAR data processing and DEM comparison. Eq. (3.25) involves two baselines and therefore will involve the states of either three or four satellites, depending if the two baselines involve one common satellite (e.g. in case $v = l$). Writing the equation in terms of the positioning error vectors results in

$$\Delta h_{uv/lw} = \frac{S_{lw}\sin(\theta)}{\rho_{\perp_{lw}}}\cdot(\Delta\vec{r}_v - \Delta\vec{r}_u)\cdot\hat{i}_{sw} - \frac{S_{uv}\sin(\theta)}{\rho_{\perp_{uv}}}\cdot(\Delta\vec{r}_w - \Delta\vec{r}_l)\cdot\hat{i}_{sw} + \epsilon_{DEM}\ , \tag{3.26}$$

where $\hat{i}_{sw}$ is unit vector in the direction of the line-of-sight, and "$\cdot$" denotes both multiplication and dot product operator, in case the operands are vector. Defining the line-of-sight components as

$$\hat{i}_{sw} = \begin{bmatrix} i_{swI} & i_{swJ} & i_{swK} \end{bmatrix}^T\ , \tag{3.27}$$

the equation can be linearized around an initial estimate of the position vectors ($\vec{r}_u$, $\vec{r}_v$, $\vec{r}_l$, $\vec{r}_w$) for all the satellites, which results in:

$$\begin{aligned}
\Delta h_{uv/lw} =& \frac{S_{uv}\sin(\theta)i_{swI}}{\hat{\rho}_{\perp_{uv}}}\Delta r_{uI} + \frac{S_{uv}\sin(\theta)i_{swJ}}{\hat{\rho}_{\perp_{uv}}}\Delta r_{uJ} + \frac{S_{uv}\sin(\theta)i_{swK}}{\hat{\rho}_{\perp_{uv}}}\Delta r_{uK} \\
&- \frac{S_{uv}\sin(\theta)i_{swI}}{\hat{\rho}_{\perp_{uv}}}\Delta r_{vI} - \frac{S_{uv}\sin(\theta)i_{swJ}}{\hat{\rho}_{\perp_{uv}}}\Delta r_{vJ} - \frac{S_{uv}\sin(\theta)i_{swK}}{\hat{\rho}_{\perp_{uv}}}\Delta r_{vK} \\
&- \frac{S_{lw}\sin(\theta)i_{swI}}{\hat{\rho}_{\perp_{lw}}}\Delta r_{lI} - \frac{S_{lw}\sin(\theta)i_{swJ}}{\hat{\rho}_{\perp_{lw}}}\Delta r_{lJ} - \frac{S_{lw}\sin(\theta)i_{swK}}{\hat{\rho}_{\perp_{lw}}}\Delta r_{lK} \\
&+ \frac{S_{lw}\sin(\theta)i_{swI}}{\hat{\rho}_{\perp_{lw}}}\Delta r_{wI} + \frac{S_{lw}\sin(\theta)i_{swJ}}{\hat{\rho}_{\perp_{lw}}}\Delta r_{wJ} + \frac{S_{lw}\sin(\theta)i_{swK}}{\hat{\rho}_{\perp_{lw}}}\Delta r_{wK} + \epsilon_{\mathrm{DEM}}\ .
\end{aligned} \tag{3.28}$$

Defining the term

$$\mathrm{D}_{uv} = \begin{bmatrix} \frac{S_{uv}\sin(\theta)i_{swI}}{\hat{\rho}_{\perp_{uv}}} & \frac{S_{uv}\sin(\theta)i_{swJ}}{\hat{\rho}_{\perp_{uv}}} & \frac{S_{uv}\sin(\theta)i_{swK}}{\hat{\rho}_{\perp_{uv}}} & 0 \end{bmatrix}\ , \tag{3.29}$$

the line of the design matrix corresponding to the DEM height offset for the pairs of baseline ρ_{uv} and ρ_{lw}, assuming that $u < v < l < w$, is given by

$$\mathrm{A}_{\mathrm{D}uv} = \begin{bmatrix} \mathbb{0}_{4(u-1),1} \\ \mathrm{D}_{uv}^T \\ \mathbb{0}_{4(v-u-1),1} \\ -\mathrm{D}_{uv}^T \\ \mathbb{0}_{4(l-v-1),1} \\ -\mathrm{D}_{lw}^T \\ \mathbb{0}_{4(w-l-1),1} \\ \mathrm{D}_{lw}^T \\ \mathbb{0}_{4(n-w)+N,1} \end{bmatrix}^T\ . \tag{3.30}$$

Assuming one satellite is common to both baselines or, without loss of generality, that

$u < v = l < w$, the corresponding line of the design matrix is given by

$$\mathrm{A}_{\mathrm{D}uv} = \begin{bmatrix} \mathbb{0}_{4(u-1),1} \\ \mathrm{D}_{uv}^T \\ \mathbb{0}_{4(v-u-1),1} \\ -\mathrm{D}_{uv}^T - \mathrm{D}_{vw}^T \\ \mathbb{0}_{4(w-v-1),1} \\ -\mathrm{D}_{vw}^T \\ \mathbb{0}_{4(n-w)+N,1} \end{bmatrix}^T . \tag{3.31}$$

The number of measurements available correspond to the number of independent pairs of baselines, and it grows rapidly with the number of satellites in the formation. Given n SAR satellites flying in formation, the number of baselines that can be formed from those satellites is given by

$$N_{\text{baselines}} = \frac{n(n-1)}{2} . \tag{3.32}$$

The number of different pairs of baselines is given by

$$N_{\Delta h} = \frac{n(n-1)}{4} \left[\frac{n(n-1)}{2} - 1 \right] . \tag{3.33}$$

Similarly to the inter-satellite ranging case, the final estimator is be obtained by appending the DEM height offsets and the lines $\mathrm{A}_{\mathrm{D}uv}$ from every combination of baseline to the measurement error matrix $\Delta\mathrm{Y}$ and the design matrix A in Eqs. (3.7) and (3.12) from the first test case.

Assuming that all the systems are identical so that the expected additive noise level is the same for every pair of satellites, the covariance matrix of the measurements vector is given by

$$\mathrm{Q} = \begin{bmatrix} \sigma_P \cdot \mathbb{1}_{2N,2N} & \mathbb{0}_{2N,N_{\Delta h}} \\ \mathbb{0}_{N_{\Delta h},2N} & \sigma_{\mathrm{DEM}} \cdot \mathbb{1}_{N_{\Delta h},N_{\Delta h}} \end{bmatrix} \tag{3.34}$$

Note that the SAR systems combine data acquired in a continuous time interval to form the synthetic aperture. In the equations developed in this section, it is assumed that the baseline error affecting the interferogram remains constant for the SAR image acquisition time. This assumption is based on the fact that the baseline error for two identical satellites flying at close distance experience almost the same gravity field and are exposed to highly correlated orbital perturbations, and hence show high degree of temporal correlation [KMF$^+$07].

3.2 Simulation framework

Figs 3.7 and 3.6 Illustrate the two orbit configurations tested. The trajectories are expressed in Clohessy Witshire (CW) frame relative to a reference satellite, here denominated as Chief. The first configuration consists in a series of satellites flying in very close formation with almost identical orbits, separated by a fixed distance. In the second configuration two of the satellites describe a elliptical trajectory around the reference satellite, and one describes a linear pattern, oscillating in the vertical direction. In this configuration the orbit geometries are highly variable. Each of the algorithms described in section 3.1 are run for both configurations and for an increasing number of satellites, varying from 2 to 4.

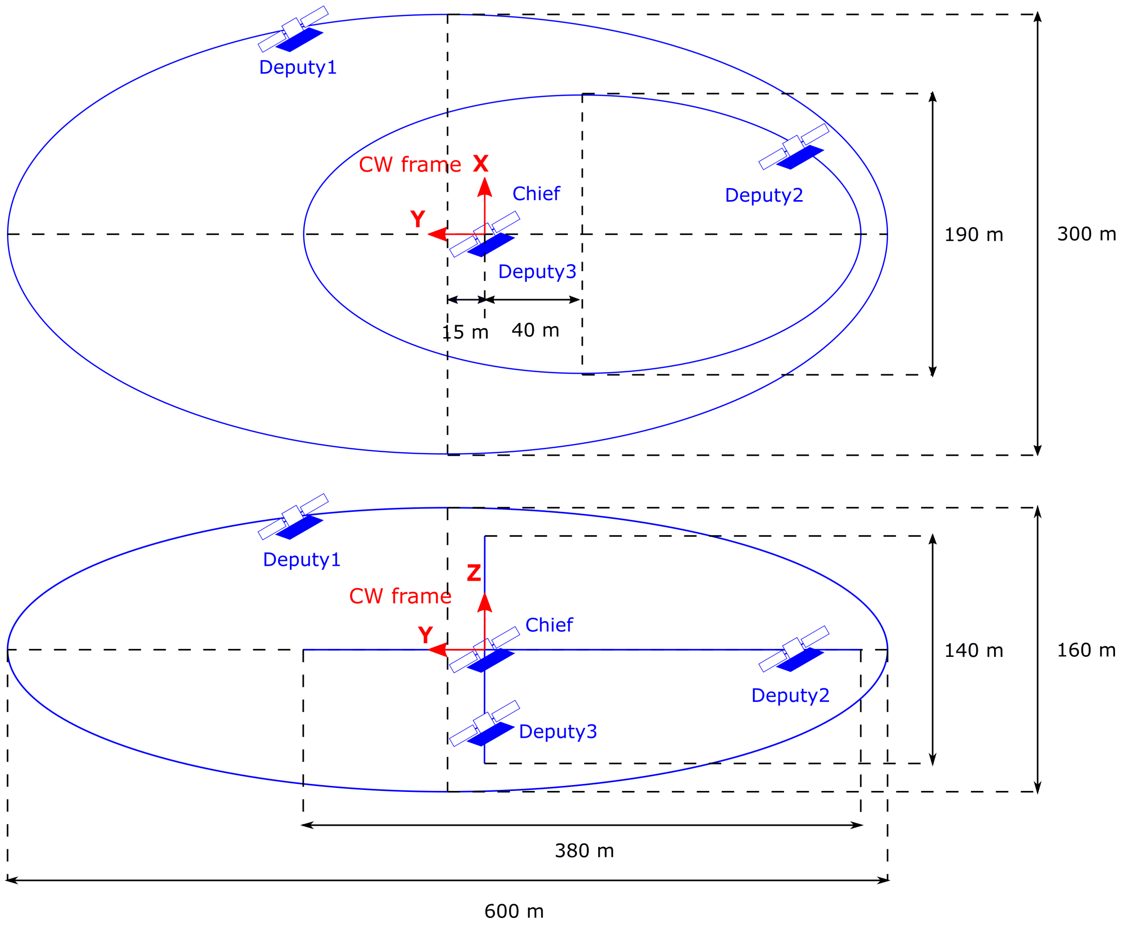

Figure 3.6: Test constellation in helix configuration. The trajectories in CW frame are indicated in blue.

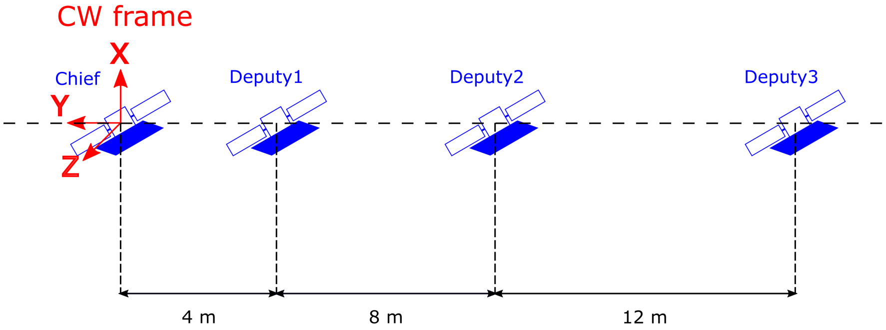

Figure 3.7: Test constellation in train configuration. The trajectories in CW frame are indicated in blue.

The simulation framework is illustrated in Figs. 3.9 and 3.8. The SAR trajectories are simulated using the software General Mission Analysis Tool (GMAT) from NASA. Although the algorithms and the conclusion apply to any GNSS constellation or combination of constellations, the simulation was based on the GPS constellation, which is the most used GNSS constellation. The position data for the GPS constellation was imported and propagated from real TLE data using the software Systems Tool Kit (STK) from AGI. Both GMAT and STK are mission analysis tools widely used in the space industry. The simulated trajectory data for the SAR constellation and from the GPS constellation are imported into a python environment and all the measurements are simulated based on the position vectors. The GNSS data is simulated according to Eqs. (2.12) to (2.13), and (2.15) to (2.16). The inter-satellite range is simulated according to Eq. (3.17) and the DEM height biases according to Eq. (3.24). Note that both the code delay and the phase delay are simulated, although only the code delay is used in this section. The phase delay measurements will be used in the following section. The simulated data serve as input for sub-routines implementing the estimation algorithms described in the previous sections. Table (3.1) details the parameters used for the simulation.

The receiver parameters are based on the Phoenix GPS receiver from the German Space Operations Center (GSOC) [MR], except that the theoretical receiver here considered is dual frequency capable while the Phoenix receiver is not. The simulated inter-satellite ranging precision is chosen to be five times worse than the one reported for GRACE mission [Kro06], an expensive state-of-the-art system. The standard deviation of the DEM elevation is based on results from the TanDEM-X mission [GAB$^+$12]. The clock delays are modelled by a uniform probability distribution between zero to a maximum level. The maximum value is in accordance with reported delay values for GPS receivers.

Table 3.1: Simulation parameters for positioning determination tests.

Parameter	Value
GNSS L1 signal frequency	1575.42 MHz
GNSS L2 signal frequency	1227.6 MHz
Code delay measurement standard deviation	0.4 m
Phase delay measurement standard deviation	0.5 mm
Inter-satellite ranging standard deviation	0.005 mm
DEM relative height standard deviation	1.8 mm
GNSS position bias standard deviation	2.0 m
Minimum elevation for visibility	10°
Vertical Total Electron Content (VTEC)	50 TECU
Maximum clock delay	0.1 nanoseconds
Chief satellite altitude	500 km
Chief satellite inclination	80°
SAR incidence angle	45°
Simulation time	24 h
Simulation time step	60 minutes

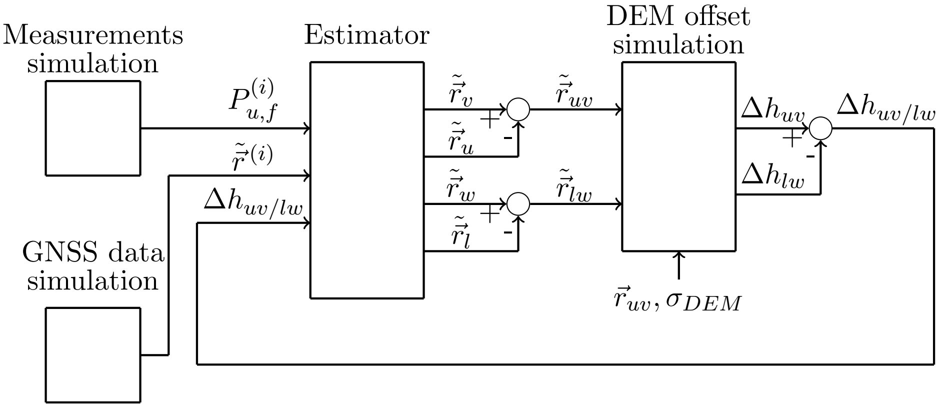

Figure 3.8: Simulation framework for DEM calibration algorithm.

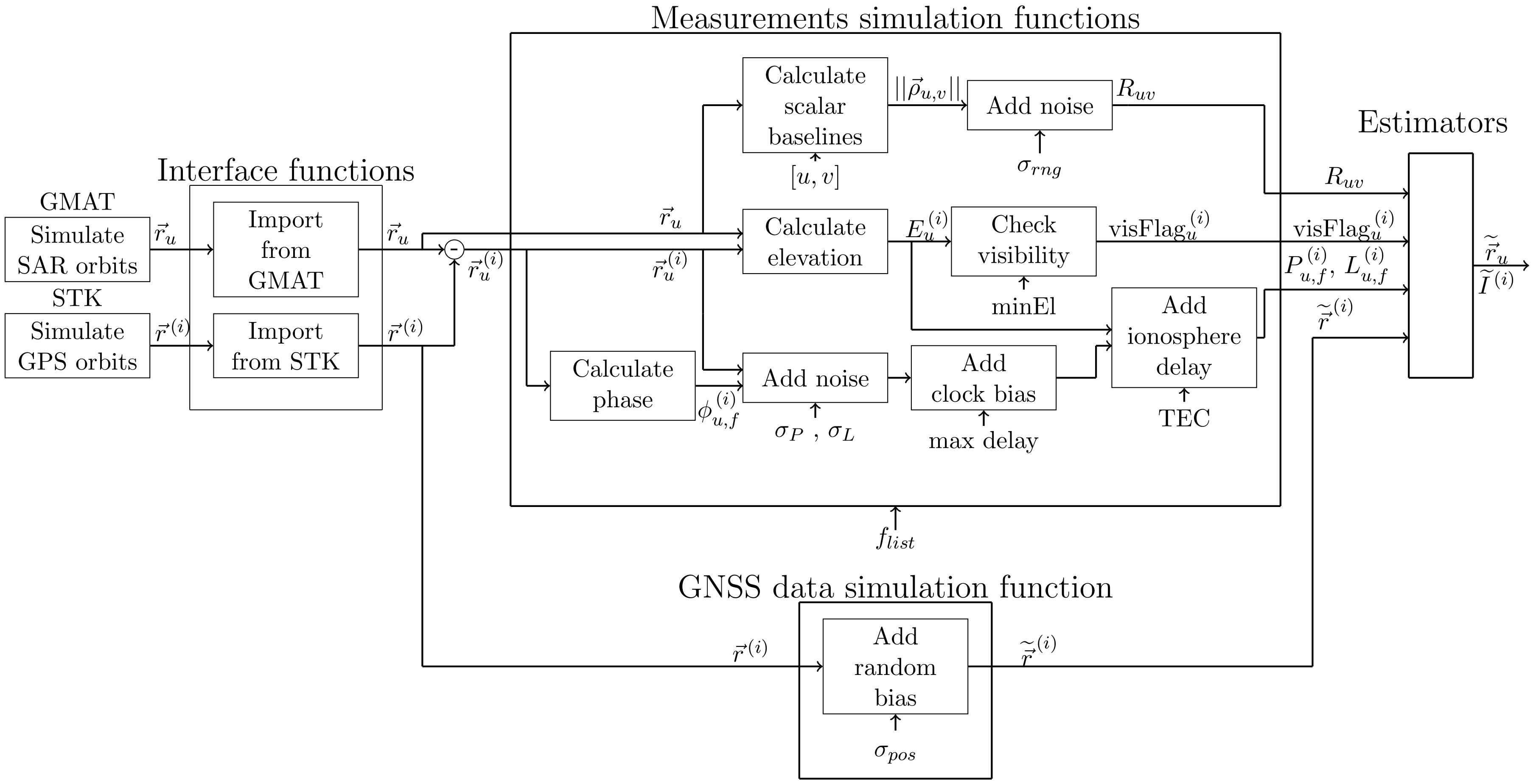

Figure 3.9: Simulation framework for testing position determination algorithms.

3.3 Estimation results

The simulation results for the baseline determination and position determination are compiled in Figs. 3.10 to (3.13). Each point in the plot represents the standard deviation of the estimated position or baseline errors for a specific spacecraft or pair of spacecrafts. Each standard deviation is calculated relative to a set of 1440 estimations taken from an orbit simulation of 24 hours duration and one minute time step. The baselines are calculated by subtracting the position vectors coherently estimated in a Linear Least Square Estimator. The results are all expressed in the CW frame relative to the chief satellite's orbit.

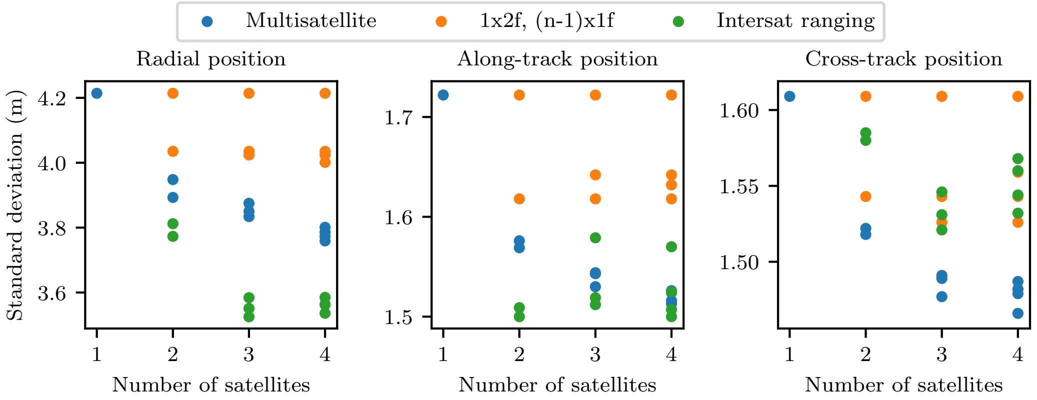

Figure 3.10: Results of position determination of satellites in train configuration.

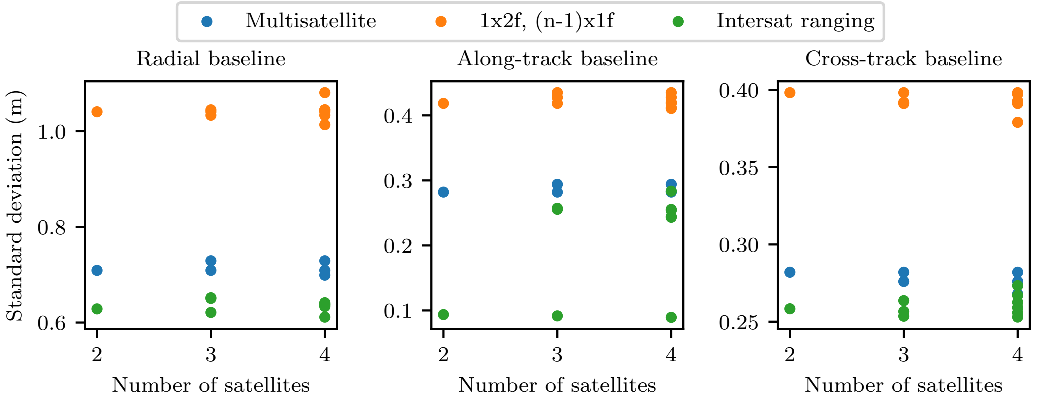

Figure 3.11: Results of baseline determination of satellites in train configuration.

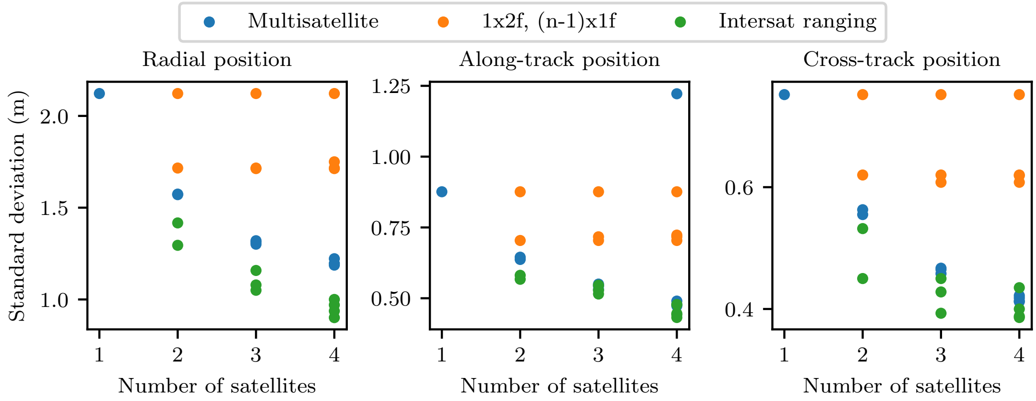

Figure 3.12: Results of position determination of satellites in helix configuration.

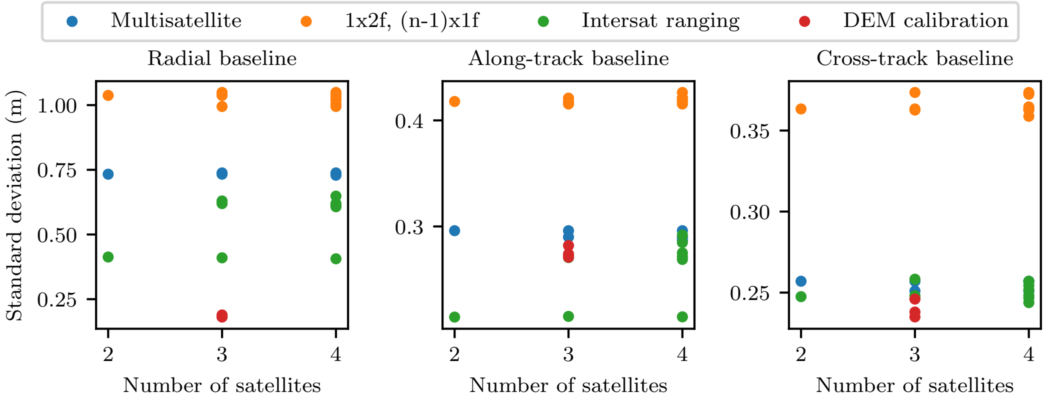

Figure 3.13: Results of baseline determination of satellites in helix configuration.

The position accuracy improves with the number of satellites for all the cases in which all the satellites are equipped with dual frequency receivers, except for an outlier in the along-track direction for the helix configuration and four satellites. In these cases each satellite adds a new independent measurement of the ionospheric delay, thus more satellites results in better ionospheric delay estimation and overall better accuracy. The gains in accuracy, however, decrease at each satellite addition. To understand this diminishing gain, consider the simplest estimation case, in which a variable is estimated by measurements described by the variable's true value plus a zero-mean Gaussian process. In this case, the variance of the estimation is inversely proportional to the square root of the number of measurements. In the first scenario, since the estimated common variable is not directly measured, it is expected that the performance will be worse than the one in the simplest estimation case aforementioned, which already presents diminishing gain.

This hypothesis is confirmed by the results.

As for the baselines, none of the results shows improvement with the number of satellites. This is due to the fact that in all cases, except the DEM calibration, the only estimation parameter which improves with the number of satellites is the ionospheric delay, which has negligible influence in the baseline for satellites at close proximity. The DEM height offset does offer additional information on the baseline at each satellite addition. The DEM calibration test, however, worked only for the case with three satellites, and therefore it's not possible confirm from the results if the baseline estimate would improve by adding more satellites.

The case in which one satellite is equipped with a dual frequency receiver and the others with single frequency receivers shows comparable results, albeit consistently inferior, to the case in which all satellites have dual frequency receivers. The fact that there is no major discrepancy between the performances in those cases reinforces the idea that sufficiently good results can be achieve by employing dual frequency receivers in only a few of the satellites in the formation.

The case in which every satellite is equipped with dual frequency receivers and two of them share inter-satellite ranging system shows better results in both the position and in the baseline compared to the base scenario. The baseline between the satellites sharing the ranging system is considerably better than the others, but the introduction of the inter-satellite link also affects other baselines. The baseline determination is better for inter-satellite link with in helix configuration compared to the train configuration, which indicates that the performance of the estimation in this case depends on the geometry of the formation.

Only the case with three satellites and helix configuration improved with the introduction of DEM height offset data. The other cases either diverged or converged to solutions hundreds of meters away from the true value. This is possibly due to the fact that the DEM height offset is highly sensitive to the baseline error, and errors on the order of several decimeters in the results are not appropriate for interferometric applications. In the case with four satellites, the number of relative height offset measurements greatly increases, and those measurements end up outweighing the GNSS code delay measurements in the estimator and leading the estimator to a local minimum far from the true value. The consistent improvement observed for the case with three satellites and helix configuration, however, indicates that the idea has great potential, especially because it doesn't require any additional hardware. Finally, the results show improvement for every component of the baseline compared to the base scenario, but in particular for the component in the radial direction.

It should be noted that in a real case the DEM combinations from different satellites are expected to correlated to some degree, as they are derived from the same sets of SAR data. This correlation was not considered in the model here presented. In addition it is unclear how the fact that the DEM offset is assigned to a single instant in time will affect the results in a real case. As mentioned before, the interferogram are formed with data from an a interval of time, not from a single instant. These two factors may play an important role if the DEM height calibration scheme is applied to real data.

These gaps should be further investigated. One possibility of evaluating their effects on the result is by implementing the technique with dynamic estimation algorithms, which relates data from different instants in time, and by adding some level of correlation to the measurements.

Concluding this section, we notice potential in most of the ideas presented here. The inter-satellite ranging and the DEM calibration scenarios show potential to improve the baseline results, and the case using only one double-frequency receiver shows potential of achieving acceptable precision with a cheaper system design. The case in which only data from dual-frequency receivers is used shows no improvement on the baseline by processing data from several satellites in the same estimator.

4 GNSS and POD-based phase synchronization

This chapter puts forward an approach to estimate the oscillator phase errors in bistatic and multistatic SARs, based on GNSS phase delay data and on baseline estimates from Precise Orbit Determination (POD), provided both the radar and the navigation receiver share the same master oscillator. The approach exploits the fact that the phase drift of the oscillator in the navigation receiver needs to be estimated in the standard navigation solution. This drift directly affects the pseudorange measurements between the GNSS satellite and the GNSS receiver, in the form of a clock bias, and is estimated with the position and velocity in a filter. The suggested approach links the synchronization and navigation solutions.

The chapter presents a detailed error analysis, and evaluates the impact of all systematic components in the solution. It is organized in five sections: Section 4.1 describes the proposed synchronization solution based on POD and GNSS data; Section 4.2 presents an error analysis, detailing all the factors that affect the phase estimation precision; Section 4.3 presents a method for integrating data from a synchronization link, such as the one employed in TanDEM-X mission, with the navigation-based synchronization; Section 4.4 presents the end-to-end simulation used to validate the analysis in a representative scenario; Section 4.5 closes the chapter with a discussion on the simulation results.

4.1 POD-based synchronization approach

Figure 4.1 shows the block diagram of a possible, most general, GNSS-based architecture for the solution of the considered synchronization problem. The same Ultra Stable Oscillator (USO) is used for generating the radar signal and the reference signal in the GNSS receiver. The natural frequency of the master oscillator is up-converted accordingly for both radar and GNSS receiver. Without loss of generality, we will assume in our analysis that both radar and navigation carriers are a multiple of the master frequency of the system. Note the block diagram of Fig. 4.1 incorporates a full-duplex direct link as used for the synchronisation of the TanDEM-X instruments [KMF$^+$07]. The proposed solution does not depend on this link, but they can complement each other, as will be explained in Section 4.3.

The phase difference of the raw data of the GNSS receivers of the two spacecraft carries information on the phase noise of the radar signal. This information, however, comes mixed with the delay from the GNSS satellites to the SAR satellite in addition to

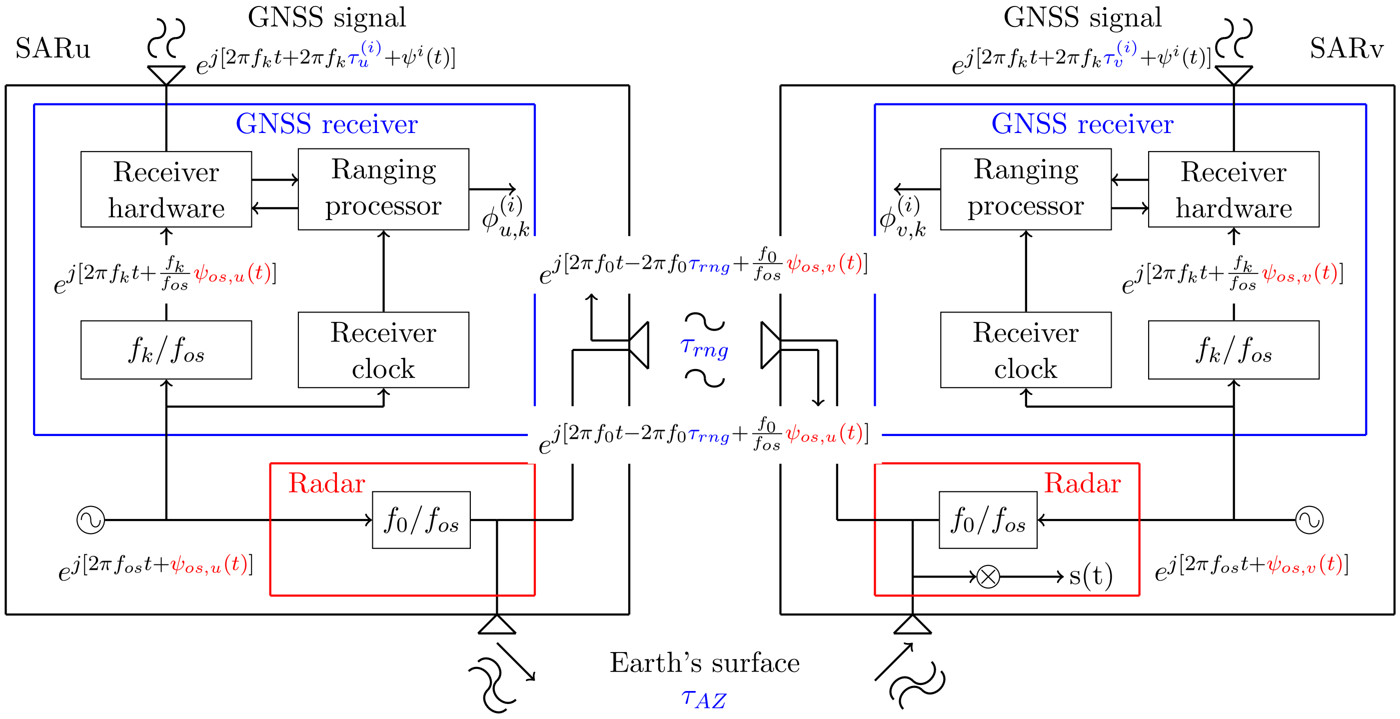

$$\text{SAR signal: } s(t) = \exp[j\tfrac{f_0}{f_{os}}[\overbrace{-2\pi f_{os}\tau_{AZ}}^{\text{AZ modulation}} + \overbrace{\psi_{os,u}(t-\tau) - \psi_{os,v}(t)}^{\text{phase noise}}]$$

$$\text{GNSS carrier phase difference: } \phi_{uv,k}^{(i)} = 2\pi\left[f_k\left(\tau_v^{(i)} - \tau_u^{(i)}(t)\right) + A_v^{(i)} - A_u^{(i)}\right] + \tfrac{f_k}{f_{os}}\left(\psi_{os,v}(t) - \psi_{os,u}(t)\right)$$

$$\text{Direct link phase difference: } \phi_{r,uv}(t) = \tfrac{f_k}{f_{os}}\left(\psi_{os,v}(t) - \psi_{os,u}(t)\right)$$

Figure 4.1: Proposed hardware configuration for radar phase synchronization based on GNSS, also used as basis for the analysis. In this figure, $\tau^{(i)}{}_{()}$ are the delays from GNSS satellite to the SAR satellites. The terms $A_{()}^{(i)}$ accounts for the ambiguity of the carrier phase measurements.

a scaling factor proportional to the ratio between the navigation and radar carriers. On the other hand, the phase difference of the raw data of the synchronization link operated at the radar carrier directly incorporates the relative phase between the received radar signals. The idea proposed in this paper is to combine the coherent processing of the raw data of the GNSS receivers of the two spacecraft with the baseline solution provided by POD. The difference between one and the other provides a scaled version of the phase offset between the received radar echoes and the internally generated signal in the receiving satellite - also called phase noise - as shown in Fig. 4.1.

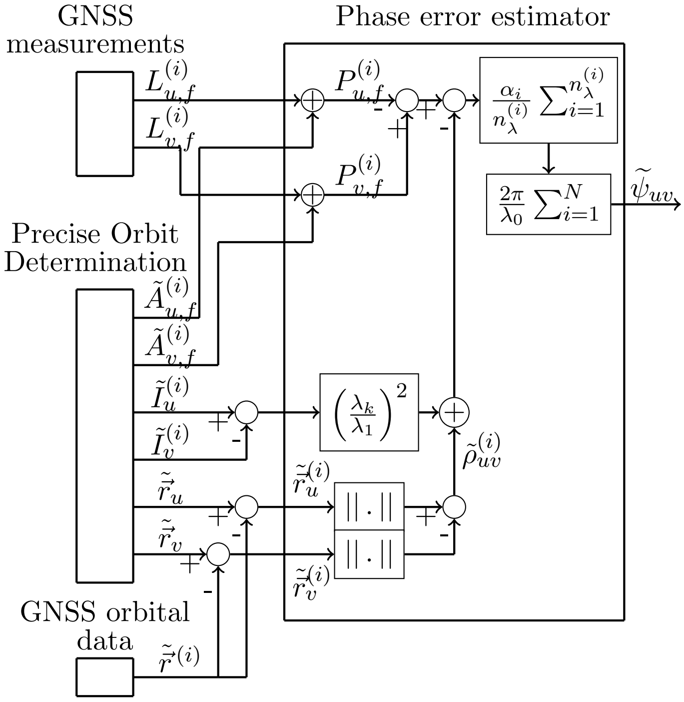

Figure 4.2: Proposed POD-based estimator of radar carriers phase difference.

The proposed estimator is shown in Fig. 4.2. The terms in this diagram are explained later in this section. It suggests a two-step approach in which the estimation of the clock synchronization phase is conducted after a regular POD process. The complete estimation (i.e., POD and clock phase) could also be done in a single step, in which both the baseline and clock phase difference are estimated simultaneously. We stick in this thesis to the two-step solution for the sake of simplicity of analysis and implementation. Employing a single-step approach is not expected to improve noticeably the accuracy of the estimation due to the different temporal scales of the clock phase noise (much faster) and the changes in spacecraft acceleration (much slower). This is illustrated in [SCFD16], which demonstrates that using data at a higher temporal sampling rate does not necessarily result in improved precision of the navigation solution, and it can even worsen it.

It is important to mention that since the same oscillator is used for the radar and for the GNSS receiver, it has to satisfy constraints for both systems. In terms of stability, radar oscillators tend to show better short-term characteristics, sometimes at the expense of long-term stability.

In the following equations in this section the lower index followed by comma as in $()_{u,k}$ indicates the navigation carrier frequency k. Furthermore, the difference between quantities is denoted as $()_{uv} = ()_v - ()_u$. The phases of the radar reference signal $\psi_{u,0}$ and of the GNSS receiver $\psi_{u,k}$ are related as follows

$$\psi_{u,0} = \frac{f_0}{f_k} \cdot \psi_{u,k}(t) = \frac{\lambda_k}{\lambda_0} \cdot \psi_{u,k}(t)\,, \tag{4.1}$$

where f_0 and is the carrier frequency of the radar, f_k is the carrier frequency of the navigation signal k, λ_0 is the carrier wavelength of the radar, and λ_k is the wavelength of the navigation signal k. Eq. (4.1) suggests any phase drift in the output of the master oscillator will be replicated in all reference signals derived from it, only scaled by the appropriate up-scaling or down-scaling factors. This assumption remains valid as long as the bandwidth of the reference signals is much smaller than the distance between the harmonics generated in the up-conversion [Poz12].

Under these circumstances, the solution of the oscillator phase noise provided by the navigation solution can be effectively used for the calibration of the phase reference of the radar data. Note that the phase noise affecting the bistatic radar measurements is the scaled version of the differences between the transmitter and receiver oscillators evaluated at times delayed by τ the two-way travel time of the radar signals, as acknowledged in [KY06]. This lag, typically in the order of milliseconds, is beyond the inverse of the bandwidth relevant for the calibration of the bistatic SAR data, which allows us to approximate

$$\psi_v(t-\tau) - \psi_u(t) \approx \psi_v(t) - \psi_u(t)\,, \tag{4.2}$$

where the subscript 0 referring to the radar carrier has been omitted for compactness, and subscripts v and u can be identified with receiver and transmitter, respectively.

Let us assume each radar unit u and v incorporates its own GNSS receiver triggered by the radar oscillator as described in Fig. 4.1. A biased measurement of the distance between the GNSS receiver and the GNSS satellite can be derived from the code delay $P_u^{(i)}$ or from the carrier phase measurement $L_u^{(i)}$. The former measurement is unambiguous but less accurate. The latter one is ambiguous but has a precision at least two orders of magnitude better and also a potentially better accuracy. Assuming that we can estimate the ambiguity term, a pseudorange can be calculated from the carrier phase measurement as follows

$$P_{Lu,k}^{(i)} = L_{u,k}^{(i)} + \lambda_k \cdot \tilde{A}_{u,k}^{(i)}\,, \tag{4.3}$$

where the term $\lambda_k \cdot \tilde{A}_u^{(i)}$ corresponds to an estimate of the true ambiguity $\lambda_k \cdot A_u^{(i)}$. For the remainder of this chapter, the pseudorange measurement is considered to be obtained from the carrier phase as shown in Eq. (4.3), since it provides a much higher accuracy as long as the ambiguity term can be accurately determined.

The relationship between the differences of the pseudoranges $P_{Luv,k}^{(i)}$ and the clock biases expressed in time δt_{uv} is given by [Kro06]

$$P_{Luv,k}^{(i)} = \rho_{uv}^{(i)} + \mathrm{c} \cdot \delta t_{uv} - \left(\frac{\lambda_k}{\lambda_1}\right)^2 \cdot I_{uv}^{(i)} + \epsilon\,, \tag{4.4}$$

where $\rho_{uv}^{(i)}$ is the difference between the distances from receivers v and u to the i-th navigation satellite, respectively, $I_{uv}^{(i)}$ is the difference between the biases caused by the ionospheric delays for the wavelength λ_1, and ϵ is the measurement error, which includes systematic and noise-like contributions such as the thermal noise in the receivers and the ambiguity estimation errors. A closer look into the physical effects contributing to ϵ is given in Section 4.2. By isolating the clock bias term we can identify the relationship between the navigation data and the clock synchronisation solution as follows

$$\mathrm{c} \cdot \delta t_{uv} = \frac{\lambda_0}{2\pi} \cdot \psi_{uv,0} = P_{Luv,k}^{(i)} - \rho_{uv}^{(i)} + \left(\frac{\lambda_k}{\lambda_1}\right)^2 \cdot I_{uv}^{(i)} - \epsilon\,. \tag{4.5}$$

An estimator of the clock synchronization solution can be derived from Eq. (4.5) using a weighted average over all navigation satellites in sight (i.e., N) and all the $n_\lambda^{(i)}$ received GNSS frequencies as

$$\tilde{\psi}_{uv,0} = \frac{2\pi}{\lambda_0} \cdot \sum_{i=1}^{N} \sum_{k=1}^{n_\lambda^{(i)}} \alpha_i \cdot \frac{P_{Luv,k}^{(i)} - \tilde{\rho}_{uv}^{(i)} + \left(\frac{\lambda_k}{\lambda_1}\right)^2 \cdot \tilde{I}_{uv}^{(i)}}{n_\lambda^{(i)}}\,. \tag{4.6}$$

The terms in Eq. (4.6) are defined as follows: $\tilde{\rho}_{uv}^{(i)}$ is the estimated value of $\rho_{uv}^{(i)}$ as provided by POD through direct estimation or through interpolation; α_i are the weights for the signal from each navigation satellite according to its quality (e.g., signal-to-noise ratio); $\tilde{I}_{uv}^{(i)}(t)$ is the estimated differential ionospheric delay, which can be also derived in the POD process;

Eq. (4.6) provides an unbiased estimation under the assumption that ϵ is a zero-mean uncorrelated noise process. As mentioned before, ϵ contains systematic error components which will bias the estimate. When possible, these components shall be estimated and removed. It should also be noted that the terms in the second sum have been assumed to be sampled according to the condition in Eq. (4.2).

Assuming the measurement are statistically independent Gaussian processes, α_i which minimizes the variance of the estimator is given by

$$\alpha_i = \frac{\sigma_i^{-2}}{\sum_{k=1}^{N} \sigma_k^{-2}}\,. \tag{4.7}$$

where the σ_i correspond to the standard deviation of the measurements. Assuming that the measurement is dominated by the thermal noise in the receiver, σ_i can be expressed as a function of the carrier-to-noise ratio $(\mathrm{c}/n_0)_i$ as follows [Gro13]

$$\sigma_i \approx \sqrt{\frac{B_{\mathrm{L-CA}}}{(\mathrm{c}/n_0)_i}}\,, \tag{4.8}$$

where $B_{\mathrm{L-CA}}$ is the so-called tracking bandwidth of the GNSS receiver for a Phase Lock Loop discriminator. Replacing Eq. (4.8) into Eq. (4.7) yields

$$\alpha_i \approx \frac{(\mathrm{c}/n_0)_i}{\sum_{k=1}^{N} (\mathrm{c}/n_0)_k}\,. \tag{4.9}$$

In order to use this equation in a practical application, the GNSS receiver employed must be able to provide the carrier to noise ratios.

4.2 Error analysis

For the sake of clarity, the previous section provides a simplified model of GNSS observables. An error analysis demands a more realistic model incorporating the several systematic components that contribute to the error in the pseudoranges. From Eq. (2.18) the difference between the carrier phase measurements of receivers u and v is given by

$$L_{uv,k}^{(i)}(t) = \rho_{uv}^{(i)}(t) + \mathrm{c}\cdot\delta t_{uv}(t) - \left(\frac{\lambda_k}{\lambda_1}\right)^2 \cdot I_{uv}^{(i)}(t) - \lambda_k \cdot A_{uv,k}^{(i)} + M_{uvL,k}^{(i)}(t) + \epsilon_{uv,k}^{(i)}(t)\,, \tag{4.10}$$

in which t is a temporal variable, $A_{uv}^{(i)}$ is the difference between the ambiguities, $M_{uv}^{(i)}(t)$ describes other systematic error components including multipath, and a bias on the receiver tracking channel, and $\epsilon_{uv}^{(i)}(t)$ is a thermal noise process of the differenced measurement. Eq. (4.10) is valid under the assumption that the measurements at two different satellites are sampled at approximately the same epoch and the positioning and timing errors due to temporal misalignment are negligible compared to the other error sources. A similar condition applies for precise baseline determination.
Replacing Eq. (4.10) into Eq. (4.3), the pseudorange used in the estimation becomes

$$\begin{aligned} P_{Luv,k}^{(i)}(t) =& \rho_{uv}^{(i)}(t) + \mathrm{c}\cdot\delta t_{uv}(t) - \left(\frac{\lambda_k}{\lambda_1}\right)^2 \cdot I_{uv}^{(i)}(t) + M_{uvL,k}^{(i)}(t) \\ &+ \lambda_k \cdot \left(\tilde{A}_{uv,k}^{(i)} - A_{uv,k}^{(i)}\right) + \epsilon_{uv,k}^{(i)}(t)\,. \end{aligned} \tag{4.11}$$

A further elaboration of the system model suggests the incorporation of independent phase noise realizations occurring in the up-conversion stages of the radar and navigation receiver electronics, which may be in principle different for each navigation frequency. Under these circumstances, we can relate the phase differences at radar and navigation carriers between the two satellites as follows

$$\psi_{uv,0}(t) = \frac{\lambda_k}{\lambda_0} \cdot \left[\psi_{uv,k}(t) + \Delta\psi_{uv,k}(t)\right] , \tag{4.12}$$

where $\Delta\psi_{uv,k}$ denotes the additional phase noise introduced in the up-conversion stages for the radar and navigation carriers at the level of the latter.

The error in the estimation of the differential phase at the radar carrier can be derived after combining (4.6), (4.11) and (4.12) as follows

$$\begin{aligned}\delta\psi_{uv,0}(t) =& \sum_{i=1}^{N} \sum_{k=1}^{n_\lambda^{(i)}} \frac{2\pi \cdot \alpha_i}{\lambda_0 \cdot n_\lambda^{(i)}} \cdot \left\{ \frac{\lambda_k}{2\pi} \cdot \Delta\psi_{uv,k}(t) + \left[\rho_{uv}^{(i)}(t) - \tilde{\rho}_{uv}^{(i)}(t)\right] + \lambda_k \cdot \left(A_{uv,k}^{(i)} - \tilde{A}_{uv,k}^{(i)}\right) \right. \\ & \left. + M_{uvL,k}^{(i)}(t) - \left(\frac{\lambda_k}{\lambda_1}\right)^2 \cdot \left(I_{uv}^{(i)}(t) - \tilde{I}_{uv}^{(i)}(t)\right) + \epsilon_{uv,k}^{(i)}(t) \right\} .\end{aligned} \tag{4.13}$$

Note that since the error components are proportional to the inverse of the radar wavelength, the estimation error increases with the radar frequencies. Each term within curly brackets in 4.13 describe an error component of the POD-based estimation of the radar synchronization phase, averaged over all tracked GNSS signals and scaled by the corresponding radar wavelength. These error components are listed in the bullets below in the order from left to the right in Eq. (4.13):

- An up-conversion error for both the radar and navigation carriers;
- A baseline determination error arising from POD;
- An ambiguity resolution error, which is constant over a continuous tracking period for each GNSS satellite;
- A mismodeling term including multipath, phase bias on the receiver tracking channel, phase wind up and other systematic errors;
- An error in the estimation of ionospheric delay difference between satellites;
- Receiver noise.

Following subsections discuss in more detail the impact of each of those error components.

4.2.1 Thermal Noise Contribution

The thermal noise contribution determines the boundary of the performance of the algorithm in the absence of the other systematic components. Under the assumption of statistical independence and common standard deviation for all frequencies corresponding to the measurement of a given navigation satellite, the standard deviation of the phase estimator due to thermal noise is given by

$$\sigma_\epsilon = \frac{2\pi}{\lambda_0} \cdot \sqrt{\sum_{i=1}^{N} \frac{\alpha_i^2 \cdot \sigma_{uv,i}^2}{n_\lambda^{(i)}}}\,, \tag{4.14}$$

where $\sigma_{uv,i}$ is the standard deviation of the differential noise process corresponding to the signal received from the GNSS satellite i. Under the assumption that both parts receive the signal from satellite i with similar quality, quite reasonable for standard baselines and equal GNSS receivers, and substituting from Eq. (4.7), the previous expression can be approximated as

$$\sigma_\epsilon \approx \frac{2\pi}{\lambda_0} \cdot \sqrt{\frac{2}{n_\lambda}} \cdot \frac{1}{\sum_{i=1}^{N} \sigma_i^{-2}}\,, \tag{4.15}$$

where the same number of available navigation frequencies n_λ for all satellites has been assumed. Denoting $\sigma_{\phi_{min}}$ and $\sigma_{\phi_{max}}$ the minimum and maximum standard deviations among $\sigma_\phi^{(i)}$, σ_ϵ can be bounded as follows

$$\frac{2\pi}{\lambda_0}\sqrt{\frac{2}{n_\lambda N}}\sigma_{\phi_{min}} \leq \sigma_\epsilon \leq \frac{2\pi}{\lambda_0}\sqrt{\frac{2}{n_\lambda N}}\sigma_{\phi_{max}}\,. \tag{4.16}$$

The equation shows that the signal level can be reduced by increasing the number of satellites and frequencies tracked. Figure 4.3 gives an example of expected performance in terms of noise of such GNSS-based synchronization scheme for a 5.404 GHz SAR payload. The receiver performance is loosely based on the single-frequency GPS receiver Phoenix developed by the German Space Operation Center (GSOC) [MR], but assuming it would be capable of receiving a second frequency with similar performance.

The results show acceptable error levels for the whole range between the maximum and minimum noise. The noise level will be closer to the minimum or maximum depending on the particular viewing geometry between the receiver antenna and the GNSS satellites at a given instant.

Finally, the error boundary given by Eq. (4.16) does not take into account the interpolation error in case the sampling frequency of the GNSS receiver is lower than the sampling frequency of radar data. The noise boundary for the performance of the POD-based estimation of the oscillator phase, considering the interpolation error, can be expressed as

$$\sigma_\psi = \sigma_\epsilon \cdot \sqrt{\frac{B_\psi}{f_{\mathrm{GNSS}}}} \approx \frac{2\pi}{\lambda_0} \cdot \sqrt{\frac{2 \cdot B_\psi}{n_\lambda \cdot f_{\mathrm{GNSS}}}} \cdot \frac{1}{\sum_{i=1}^{N} \sigma_i^{-2}}\,, \tag{4.17}$$

where B_ψ represents the bandwidth of the oscillator phase noise relevant for the correction of the bistatic SAR data and f_{GNSS} corresponds to the rate at which the pseudoranges are made available by the GNSS receivers. The value of B_ψ depends on the character-

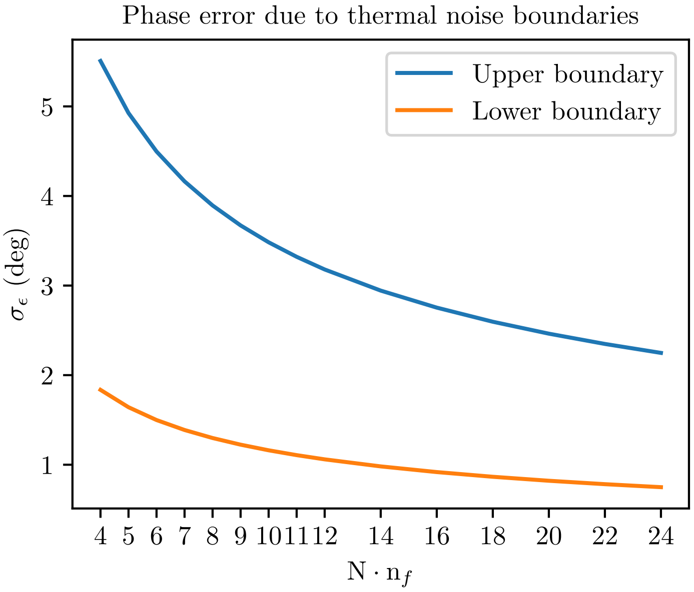

Figure 4.3: Noise boundaries for a test case for a 5.404 GHz SAR payload, with the number of satellites in view (N) varying from four to twelve and the number of frequencies n_f up to two. Receiver carrier phase estimates due to noise are assumed to vary between 1.2 and 0.4 mm.

istics of the master oscillator and of the radar carrier frequency. Reference [KMF$^+$07] evaluates the specific case of TanDEM-X, showing that values between 5 Hz and 15 Hz provide additional contributions below 0.5 and 0.1 deg, respectively.

4.2.2 Baseline determination error

This subsection presents an evaluation of the effects of the baseline error on the proposed phase synchronization. The objective is to verify the order of magnitude of this error, its dynamic behavior and how each of the three components of the baseline error - radial, along-track and across-track - affect the phase separately.

Similar to what is done in [Kro06] for direct baseline determination, the orbit determination error for each GNSS satellite can be approximated by linearizing the error term around zero as a function of the baseline solution as follows:

$$\rho_{uv}^{(i)} - \tilde{\rho}_{uv}^{(i)} \approx -\tilde{\vec{e}}_v^{(i)} \cdot \Delta\vec{r}_{uv} - \tilde{\vec{e}}_{uv}^{(i)} \cdot \Delta\vec{r}_u + \tilde{\vec{e}}_{uv}^{(i)} \cdot \Delta\vec{r}^{(i)}\,, \tag{4.18}$$

where the $\tilde{\vec{e}}_u^{(i)}$ are unit vectors indicating the direction from the estimated SAR satellite u to GNSS satellite i positions, as shown in Fig. 4.4. The terms $\Delta\vec{r}^{(i)}$, $\Delta\vec{r}_{uv}$ and $\Delta\vec{r}_u$ denote the GNSS satellite position error, the error in the baseline vector from u to v, and the error in the position of satellite u, respectively.

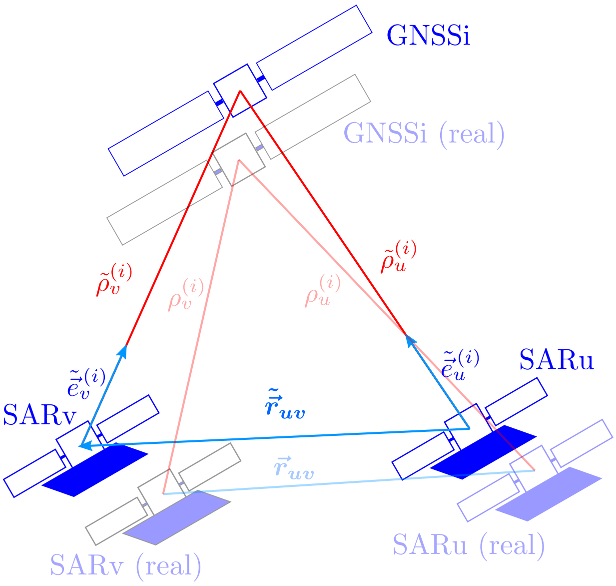

Figure 4.4: Basic geometry for the derivation of the baseline determination error.

The terms $\tilde{\vec{e}}_{uv}^{(i)} \cdot \Delta\vec{r}_u$ and $\tilde{\vec{e}}_{uv}^{(i)} \cdot \Delta\vec{r}^{(i)}$ in Eq. (4.18) are much lower compared to the first term because the vectors $\tilde{\vec{e}}_u^{(i)}$ and $\tilde{\vec{e}}_v^{(i)}$ are approximately parallel in case satellites u and v are at a close distance. For example, as demonstrated in [TK98], the term $\tilde{\vec{e}}_{uv}^{(i)} \cdot \Delta\vec{r}_u(t)$ can be bounded as follows :

$$\tilde{\vec{e}}_{uv}^{(i)}(t) \cdot \Delta\vec{r}_u(t) \leq \frac{||\vec{r}_{uv}(t)||}{||\vec{r}^{(i)}(t) - \vec{r}_v(t)||} \cdot ||\Delta\vec{r}_u||\,. \tag{4.19}$$

Assuming a baseline of 300 m, a range from SAR satellite to the GNSS satellite of

19700 km and an absolute positioning error of 1 m, the upper boundary of the term given by Eq. (4.19) is of 1.5E-2 mm, which is well below receiver noise level.

Therefore, the individual orbit determination errors can be approximated as the first term of Eq. (4.18), which yields the following expression for the total orbit determination error:

$$\sum_{i=1}^{N} \sum_{j=1}^{n_\lambda^{(i)}} \frac{2\pi \cdot \alpha_i}{\lambda_0 \cdot n_\lambda^{(i)}} \left[\rho_{uv}^{(i)}(t) - \tilde{\rho}_{uv}^{(i)}(t) \right] \approx \frac{2\pi}{\lambda_0} \Delta \vec{r}_{vu}(t) \cdot \sum_{i=1}^{N} \alpha_i \tilde{\vec{e}}_v^{(i)}(t) \,. \tag{4.20}$$

The summation on the right corresponds to a weighted average of unit vectors distributed more or less uniformly in a semi-sphere. Since the weights (α_i) depend on the signal to-noise ratio, higher elevations will be given a larger weight. Assuming an antenna pattern symmetrical with respect to the direction of the main lobe, the terms in the along track and across track in the individual vectors ($\tilde{\vec{e}}_v^{(i)}$) will tend to cancel out when taking the average. These two factors contribute to make this summation term a vector predominantly in the radial direction. Since the final result is the scalar product of the baseline error with this mostly radial vector, the radial component of the baseline error will play a more important role compared to the other components.

Figure 4.5 illustrates the influence of each component of the baseline error in the final relative phase estimated in the GNSS-based synchronization scheme. It correspond to the application of Eq. (4.20) to simulated orbital data considering a 5.404 GHz SAR payload. The GNSS orbits are obtained from propagated GPS TLE data.

Fig. (4.5) gives a general idea of the expected order of magnitude of the error resulting from the baseline error and demonstrates the higher influence of the radial component. However, it does not tell about the dynamic behavior of the phase error due to the baseline estimation. Not only the magnitude of the phase error is important, but also its temporal variation. A constant phase error can be relatively easily estimated and corrected in the SAR data processing without the need for external information. A bias which varies over time, however, will introduce artifacts in the final SAR image which are hard or impossible to compensate for. Eq. (4.20) predicts that both a variation of the average GNSS-SAR direction vector and a variation of the baseline error during the SAR data acquisition time will cause a time variation of baseline error component of the phase estimation.

The variation of the average GNSS-SAR direction vector can be evaluated from the same simulation as the one used for plotting Fig. 4.5. By checking the changes between time periods of one minute, we see that this variation remained below one second of arc and thus can be neglected.

The error in the baseline determination depends on how the real baseline changes over time compared to the estimated baseline. This error is hard to predict since it is impossible to perfectly model or measure the satellite orbital dynamics. Fortunately, the PRIMA mission offered a glimpse on this behavior. In initial mission phase, the baseline determination process was performed with the two spacecrafts attached to each other. During this phase, the true baseline could be calculated with a very high precision from

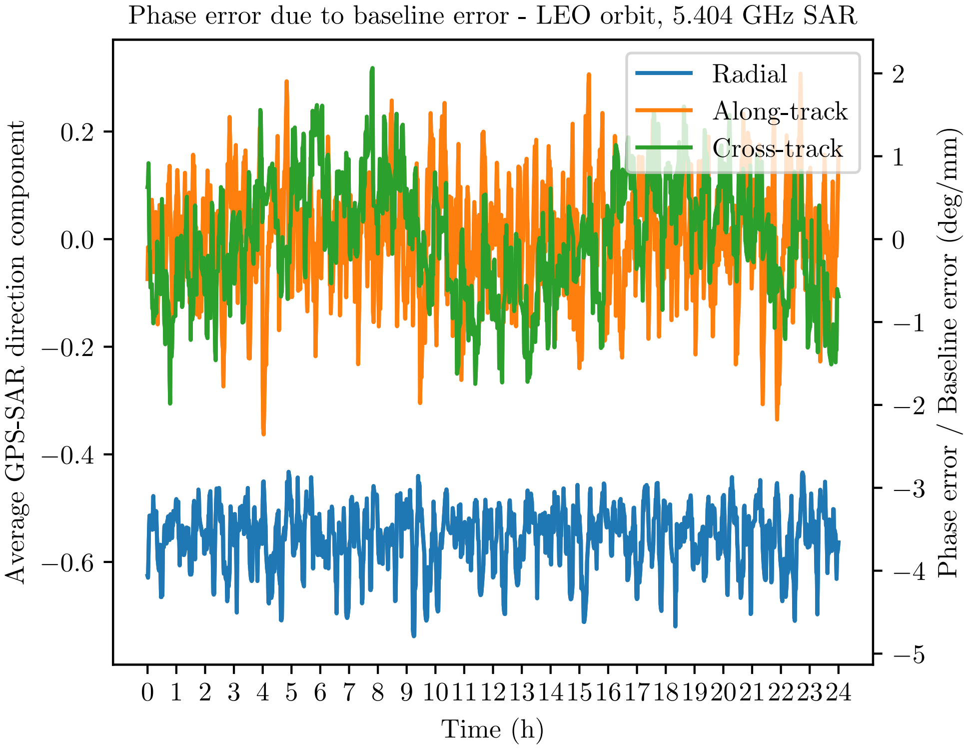

Figure 4.5: Components of the GNSS-SAR average direction vector for a 500 km altitude circular orbit and expected phase estimation error per millimeter baseline error for a 5.404 GHz SAR payload.

attitude measurements [ADM10]. A comparison between the estimated baseline through POD and the direct calculation of the baseline shows that the three components of the baseline error describe, most of the time, smooth sinus-like oscillations, with a period of around one orbital period and amplitudes of approximately 5 mm. This suggests that the baseline determination error changes smoothly and slowly enough so that it can be approximated by a linear varying term for the short time frame of one minute, in which the radar image is usually acquired. The data shows, however, a few discontinuities. These discontinuities should be avoided if possible as they would have a direct effect on the phase estimation if the scheme presented here is applied.

The simulation in the following section is roughly based on the results obtained in PRIMA mission, regarding the order of magnitude of the errors in the absolute and relative positions and velocities. It assumes an error in the initial positions and velocities, but no error in the dynamics modeling. This means that the high-order terms of the baseline error are ignored. This assumption should not affect the representativeness of the simulation since, as explained, the higher order terms of the baseline error are expected to be negligible.

4.2.3 Frequency conversion error

The upconversion error for each different frequency in the receiver can be assumed to be caused by an error in the scaling and by an additive noise ($\delta\phi_{uv,j}$):

$$\Delta\psi_{uv_k} = \left(\frac{\lambda_{os}}{\lambda'_k} - \frac{\lambda_{os}}{\lambda_k}\right)\psi_{uv,os}(t) + \delta\psi_{uv,k}(t)\,, \tag{4.21}$$

In this case, the upconversion error can be written as:

$$\sum_{i=1}^{N}\sum_{j=1}^{n_\lambda^{(i)}} \frac{\lambda_k \cdot \alpha_i}{\lambda_0 \cdot n_\lambda^{(i)}}\Delta\psi_{uv,j} = \frac{1}{n_\lambda}\sum_{j=1}^{n_\lambda}\left[\left(\frac{\lambda_j}{\lambda'_j} - 1\right)\psi_{uv,0} + \delta\psi_{uv,j}\right]. \tag{4.22}$$

An error in the multiplication factor of any of the four upconversions involved - two in each satellite - will scale the value of the estimated phase, thus causing a proportional error. Any noise introduced by those upconversions will also reflect on the final phase estimation. These errors, however, are expected to be very low. The error in the scaling, in particular, could be measured by sampling the signal before and after upconversion at an sufficiently high rate.

4.2.4 Ionospheric delay error

As mentioned before, the ionospheric delays can be estimated in the POD along with the clock bias, position and other parameters. For short baselines, of less than one kilometer, ionospheric path delays for the two satellites are expected to highly correlated. For example, in the GRACE mission, the differential path delays were dominated by carrier phase measurement noise, which resulted in a scatter of roughly 1 cm [MvYV07]. The differential ionospheric delay is thus expected to be very low and the error from the ionospheric delay estimation is expected to be even lower.

4.2.5 Mismodeling errors

In the orbit determination process the mean value of all the unmodeled errors cannot be separated from the GNSS receiver clock offset and therefore will bias it [MvYV07]. The effect of this error will cause a very slight time offset, and therefore will not affect considerably the positioning solution. For the application presented in this paper, however, these effects are critical, and the biases must be calibrated to a value low enough so that it can be corrected in the data processing.

The potentially most critical unmodeled error source is the so-called multipath effect, which results from the superposition of the GNSS signal received directly from the GNSS satellite with the signal reflected by the surfaces of the receiving satellite. This error depends on the signal difference, the strength and polarization of the reflected radiation, as well as internal characteristics of the receiver [Kro06]. The multipath effect is confined to a quarter of the navigation signal wavelength [HWLC97]. This can be a significant error and it is important for a system where Precise Orbit Determination (POD) is required, to be designed so that this effect is suppressed or avoided. For example, GRACE spacecrafts didn't employ deployable solar panels, and their mechanical layout minimizes multipath effects. PRISMA mission, which also performed experiments on POD, had the GPS antennas on the tips of the solar panels, which may have contributed to mitigate the problem of multipath effects. The strategy used in PRISMA is of particular interest for SAR missions since the high power demand in those missions may require the use of deployable solar panels.

Another relevant error source in the GNSS measurements is the so-called phase center variation. The phase centers of the receiver and transmitter antenna vary depending on their relative viewing geometry. If this variation is not accounted for, it introduces an additional error to the phase measurement. This error can be calibrated in a laboratory, as done in CHAMP and GRACE missions [MGFY$^+$09]. However, as remarked in [JDM$^+$09], even after applying the laboratory calibration, other unmodeled variations correlated with the azimuth and elevation persist. These errors can be further reduced by applying frequency-dependent patterns from on-orbit calibration. This was demonstrated in [MGFY$^+$09] through evaluation of satellite laser ranging residuals. In that work, the carrier phase accuracy was improved to a level of 4 mm, close to the pure receiver noise, by applying such frequency-dependent patterns.

In addition to the errors aforementioned, the phase measurements are affected by the so called wind-up effect, a phase accumulation due to the rotation of the antennas about the mutual line-of-sight [Kro06]. This error is not expected to be as significant as, for example, multipath errors, but it should also be considered in future analysis.

4.2.6 Ambiguities

As shown in (4.13), errors in the ambiguity estimation for each signal will affect the final phase estimate. Since the ambiguities are constant for any given tracking arc, the corresponding error component will not change as long as the receiver remains locked to the same GNSS satellites during the SAR data acquisition time. For a short acquisition time of around one minute, this will most likely be the case. If a GNSS satellite comes into view or goes out of view, using its carrier phase data would introduce a discontinuity into the relative phase estimate, which would be carried on to the final synthesized radar image or digital elevation model.

The easiest way to mitigate this problem would be to use only data from the GNSS satellites to which the receiver remained locked during the whole data acquisition period. This, however, would result in loss of useful information. One alternative solution could be to apply extra processing steps to the data specifically to identify and eliminate such discontinuities.

In the simulation in Section 4.4 this source of error is neglected, but it should taken into account in future implementations of the proposed GNSS-based synchronization scheme.

4.3 Integration of POD-based synchronization with synchronization link

Consider a system such as the one illustrated in Fig. (4.1), implementing both a inter-satellite synchronization link and the GNSS and POD-based synchronization scheme here introduced. The phase of the synchronization signal $\phi_{r_{uv}}$ received at satellite v coming satellite u can be modeled as follows:

$$\phi_{r_{uv}} = \frac{1}{c}\rho_{uv} - \lambda_0 N + \psi_{u,0} + \epsilon_{r,uv}\,, \tag{4.23}$$

where N is the number of full wavelengths between the antennas phase centers and $\epsilon_{r,uv}$ a noise component. Analogously, the synchronization phase $\phi_{r_{vu}}$ received at satellite u coming from satellite v can be modeled as:

$$\phi_{r_{vu}} = \frac{1}{c}\rho_{uv} - \lambda_0 N + \psi_{v,0} + \epsilon_{r,vu}\,. \tag{4.24}$$

Subtracting the received phases yields

$$\Delta\phi_r = \phi_{r_{vu}} - \phi_{r_{uv}} = \psi_{uv,0} + \epsilon_r\,. \tag{4.25}$$

where ϵ_r is noise process resulting from the difference between $\epsilon_{r,uv}$ and $\epsilon_{r,vu}$.

Reference [KMF+07] shows that the error in this measurement is on the order of a few degrees, which is on the same order of magnitude as the noise-like error component of the GNSS and POD-based algorithm here presented for the representative scenario evaluated in Subsection 4.2.1. Combining the two techniques, therefore, may result in a significantly better accuracy. The unbiased reference provided by the synchronization link can be used to estimate the bias and residual drift affecting the GNSS-based measurement for a better overall phase estimate.

4.4 Simulation framework

This section provides an end-to-end simulation of the POD-based estimation of a bistatic SAR operating in C band and using low-cost GNSS receivers. The purpose is to illustrate the potential of the suggested idea by providing an example of performance in a realistic scenario. The realization of the oscillator phase error used in the simulation is based on TanDEM-X calibration data, but scaled accordingly assuming a C-band SAR system. The position and baseline determination parameters are based on results from the PRISMA mission [ADM10]. The GNSS parameters are based on the Phoenix GPS receiver [MR]. The orbit geometry corresponds to the train configuration introduced in Fig. (3.7). Among the errors presented in the previous section, the ones resulting from the orbit determination and thermal noise are evaluated in the simulation. The ionospheric delay in this scenario is negligible and was therefore not taken into account in the estimator. Figure 4.6 shows the data flow and the major components of the simulation. It is based on the same simulation framework presented in Fig. (3.9).

In this case the total simulation time was of 40 seconds, representative of a SAR acquisition period, and the time step was of 1 millisecond. A C-band bistatic SAR system composed of a transmitter and receiver flying in close formation and possessing the suggested hardware configuration for POD and GNSS based phase synchronization was considered. The navigation antennas of the radar satellites have direct visibility to nine GPS satellites continuously during the simulation period. Again, the orbits of all LEO satellites are propagated using NASA's open source software GMAT, and the GPS satellites orbits are propagated from TLE data using the software STK. GMAT allows for the numerical integration of all orbits using an accurate gravitational model including drag and third bodies attraction. The errors in the position and velocity of the radar satellites coming from the precise orbit determination have been simulated by introducing an absolute bias in the initial state of the satellites and propagating the orbit. The same dynamic model is used for simulating the reference orbit and the POD result, which means that only first order terms on the baseline determination error are considered.

The error in the baseline velocity is of particular concern, since it can introduce a time-varying component in the estimated phase. The baseline error simulated was based on the reported error from the PRISMA mission when the two satellites were attached, as explained in Subsection 4.2.2.

After propagating the orbits, the ranges between the radar satellites and the GNSS satellites in view at a minimum elevation of 10 degrees are calculated. The navigation raw data are simulated by adding the following error components to the expected code and phase signal: ionospheric delay, initial clock bias, thermal noise and clock drift. The phase drift realization corresponds to a real measurement done with the synchronization link of TanDEM-X operated at a frequency of 3 kHz. The ionospheric delay is calculated assuming a constant Vertical Total Electron Content (VTEC) and applying the elevation-only dependent mapping function by Lear [Lea87]. In this case, the difference in the ionospheric delays affecting the signals in the satellites is negligible.

The simulations assume a single-frequency GNSS receiver, with noise characteristics in line with the Phoenix receiver. The error figures are in the sub-decimeter level, similar to those reported in the PRISMA mission, which also used a single-frequency GNSS receiver. The phase difference between the clocks is estimated using equation (4.7). In the case of two-frequency receivers, the residuals of the estimation are expected to improve by a factor square root of two due to the availability of a second independent measurement, in addition to the improved accuracy due to a more accurate orbit determination. Table 4.1 shows the simulation parameters.

Last but not least, the integer ambiguity factor assumed to be known from the precise orbit determination process.

Table 4.1: Simulation parameters

Parameter	Value
GNSS signal frequency	1575.42 MHz
Radar payload frequency	5405 MHz
Pseudorange standard deviation	0.0005 m
GNSS position bias standard deviation	1.5 m
Minimum elevation for visibility	10°
Number of GNSS satellites	9
Vertical Total Electron Content (VTEC)	50 TECU
Radial position error	1.478 m
Along-track position error	0.054 m
Across-track position error	-0.034 m
Radial velocity error	0.082 m/s
Along-track velocity error	0.010 m/s
Across-track velocity error	-0.007 m/s
Radial baseline error	8.248 mm
Along-track baseline error	1.177 mm
Across-track baseline error	0.767 mm
Radial baseline velocity error	0.0057 mm/s
Along-track baseline velocity error	-0.0077 mm/s
Across-track baseline velocity error	-0.0027 mm/s

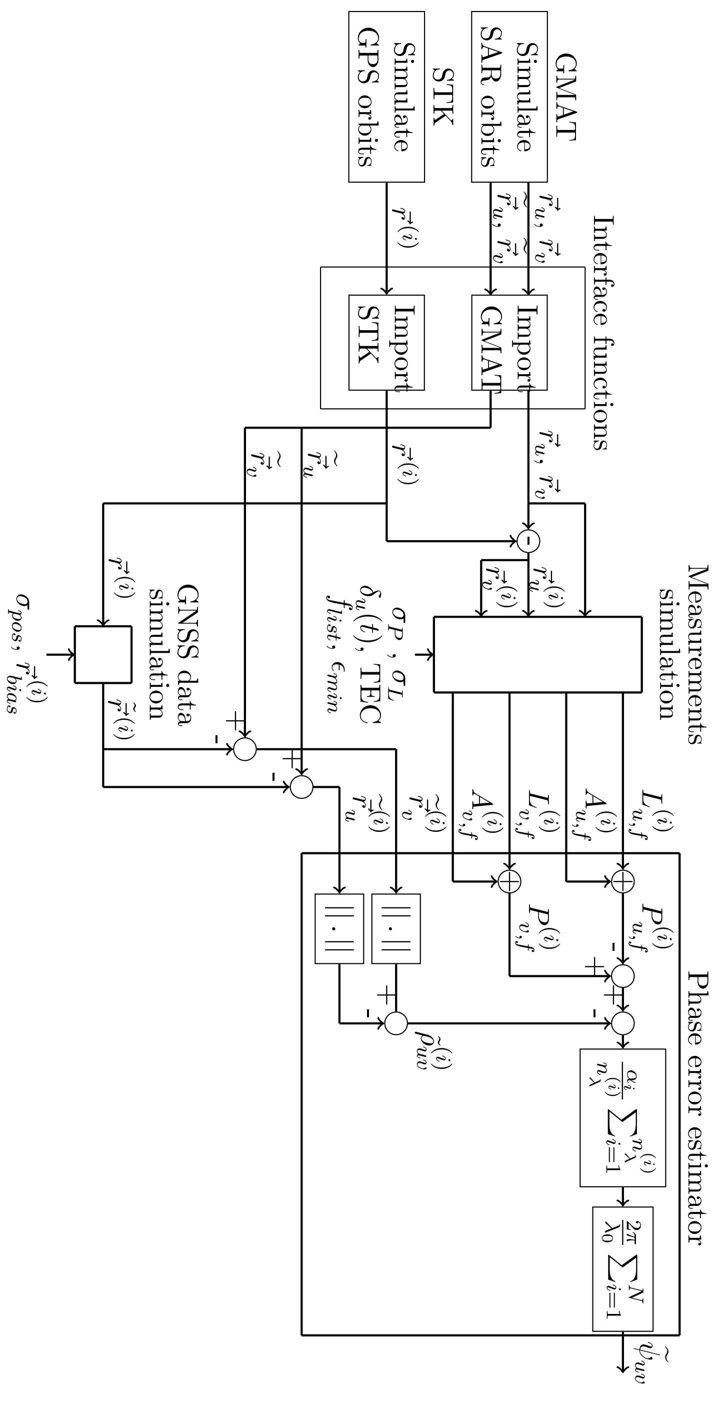

Figure 4.6: Simulation framework used to test the proposed POD-based estimation of the radar carrier synchronization phase.

4.5 Simulation results

The simulation results are shown in Figs. 4.7 and 4.8. Even though the simulation considered a single frequency receiver, compatible only with the GPS constellation, the estimated phase error curve is able to replicate well the shape of the true phase error with a standard deviation below two degrees. With hardware capable of receiving several constellations and several frequencies, the standard deviation is expected to be reduced below 1 degree. This standard deviation is of the order of magnitude of the synchronization achieved by TanDEM-X through a synchronization link [KMF$^+$07]. However, the estimate in this case is biased. This bias cannot be corrected from the GNSS data or through any method here presented but, at the level of 34.5 degrees shown in the simulation results, it can be compensated by appropriate processing of the SAR data.

The simulation demonstrates that the baseline velocity errors attained by PRISMA mission are low enough so that the linear component in the phase estimation introduced by it is below noise level.

Note that error components not considered in the estimation will affect the final accuracy result in a real scenario. In particular, the multipath effects could degrade considerably both the precision and accuracy of the solution. Unmodeled phenomena which cause errors that vary during the SAR data acquisition time are of particular concern, since their influence is harder to eliminate in the data processing.

The estimation model considered in this paper does not take into account the stochastic behavior of the radar clock. An estimator which filters the GNSS data by considering its temporal behavior might reduce the standard deviation of the phase error estimation even further. This can be inferred from Fig 4.7, which shows a clear time correlation of the relative phase bias.

The suggested solution seems to provide reliable estimates for the oscillator synchronization phase - although biased by the baseline error - as long as the contributions of the baseline velocity error, differential ionospheric delays, multipath and other systematic components are either negligible or can be corrected through appropriate calibration.

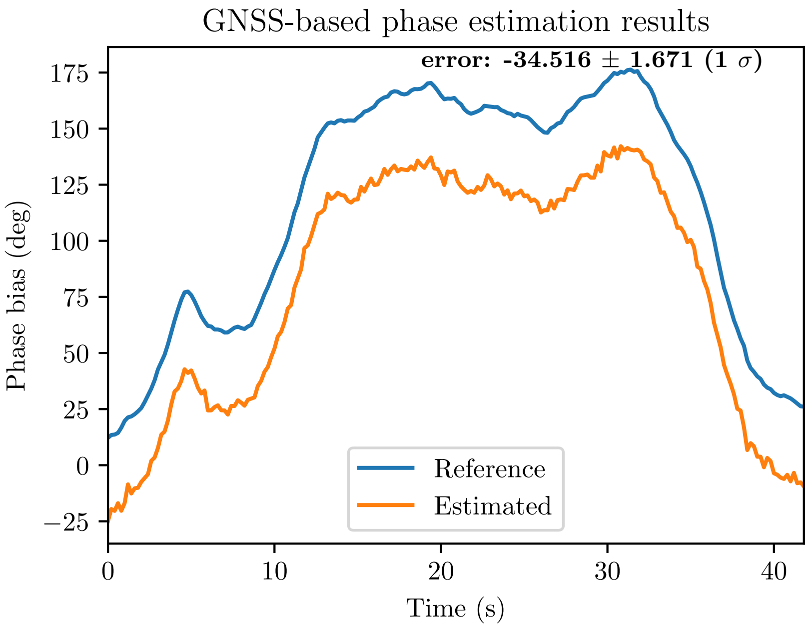

Figure 4.7: Simulated phase drift data and estimation results from multiple GNSS data.

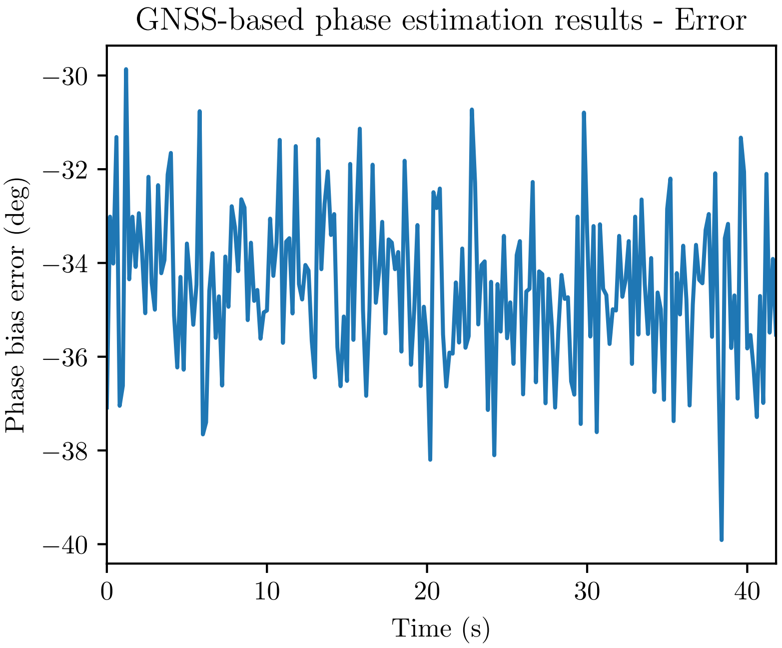

Figure 4.8: Error in the estimation from multiple GNSS data.

5 Conclusions and Outlook

5.1 Summary

This work proposes solutions using GNSS technology for bi and multistatic SAR problems, in the context of formation flight system architectures. Specifically, two SAR-related challenges are addressed: Precise baseline determination and radar phase synchronization. Precise baseline determination is necessary for SAR applications such as interferometry, and is currently achieved by employing state-of the art algorithms with expensive geodetic-grade receivers, which may pose a challenge for low-cost multi-satellite applications. Phase synchronization problems arise when the transmitter and receiver SAR satellites do not share the same platform. Phase errors, if not estimated and compensated in the data, results in artifacts in the synthetized SAR image or Digital Elevation Model (DEM), compromising their scientific value. The current operational solution for this problem uses an inter-satellite link, which adds cost, weight and complexity to the system. Therefore, a alternative solution is desirable. This thesis is divided in two major parts, each addressing one of the aforementioned problems.

The first part assesses potential ways of profiting from a SAR formation flight system architecture to improve the baseline determination accuracy. Four different scenarios were evaluated, each of them using GNSS data, some complemented with information from external hardware. In the first scenario, also referred as base scenario, only data from dual-frequency GNSS receivers is used. In the second scenario, one satellite is equipped with a dual-frequency receiver and the others with low-cost single frequency receivers. In the third scenario, data from an inter-satellite ranging system is added to the base scenario. In the fourth scenario, interferometric SAR data is used to calibrate the baseline in an iterative method. In each scenario, a kinematic position estimator based on code delay information and using data from all the satellites was formulated. A simulation framework was developed to generate the input GNSS code delay, inter-satellite ranging and interferometric data. The algorithms were applied to the simulated data for different numbers of satellites, varying from one to four. Conclusions could be drawn by comparing the results from different scenarios and for different numbers of satellites.

The second part proposes a phase synchronization scheme for bistatic and multistatic SAR systems based on GNSS navigation data, assuming that the same base oscillator is used in the GNSS receiver and in the SAR payload. A phase error estimator is proposed employing raw GNSS data and precise orbit determination data. A comprehensive error analysis was done for the estimator, including analytical evaluation of some of the main error sources. A simulation framework was developed to generate realistic input data for the proposed estimator. The simulation included POD data for the SAR satellites, position data for GNSS satellites, and raw GNSS data given by the receiver, including a clock bias drift based on real data from the TanDEM-X mission. The algorithm proposed was applied to the simulated data to evaluate the performance of the estimator in the presence of noise in the receiver and errors in the SAR and GNSS satellites orbital data.

5.2 Conclusions

The precision determination studies indicated potential for baseline determination improvement in some of the proposed scenarios. They indicated that the close proximity between satellites and the resulting high correlation between ionospheric delays could be exploited in an architecture where one satellite has a dual-frequency receiver and the others a single-frequency receiver. For the simple estimators implemented, a comparable performance for the single frequency receivers could be achieved by processing their data along with the dual-frequency receiver data. The simulations showed that using data from an inter-satellite ranging system improves the baseline accuracy, and that this improvement depends on the relative orbit geometry between the satellites. They also indicated that interferometric data can be integrated in position determination algorithms to improve the baseline accuracy in system architectures in which SAR satellites flying in formation illuminate the same area. Finally, it was demonstrated that by combining the GNSS data from several satellites flying in close proximity, under the assumption that the ionospheric delays are equal, the absolute position estimates are improved by the addition of each satellite, but not the baselines. The baselines were improved only in scenarios in which external data is combined with the GNSS data.

The estimation technique here presented offers a simple solution for the phase synchronization in bistatic or multistatic radar constellations. It has the potential for scalability, since each additional satellite designed to employ the technique can be easily integrated to the multistatic system without adding to the complexity of the other elements of the space segment. The simulations indicate that a sufficiently good performance, in terms of phase synchronization, could be obtained from low-cost GNSS receivers. The solution relies in very precise relative navigation data. It assumes that the precision is in the sub-decimeter level in relative position and negligible in relative velocity. The performance can be improved considering the recent operational readiness of the new navigation constellations Galileo and BeiDou, and with the use of receivers capable of receiving several frequencies. The error analysis indicates some critical issues which must be addressed for the technique to work. Of particular concern are multipath effects, which must be reduced to a minimum by carefully addressing the spacecraft design. Also the calibration of the up-converters must be carefully conducted in order to avoid relevant phase errors in the estimated solution. Unlike using a synchronization link, the errors of the POD-based estimation are expected to degrade -at least linearly- for increasing frequencies, and may be at the edge of usability for Ka-band radar systems.

5.3 Outlook

Given that all the positioning algorithms proposed here consisted in kinematic algorithms, a possible next step could be to implement dynamic estimators for all the scenarios considered to check if the conclusions hold for estimators closer to the ones used in real satellite operations. Furthermore, algorithms using the phase delay in addition to the code delay could be implemented. The scenarios, in particular the one using one dual frequency receiver and several single-frequency receivers, should be re-tested with a more realistic ionospheric delay model, taking in consideration the space and time variations of the ionosphere. By doing so, one can test what are the distance limits to have a ionospheric delay sufficiently correlated to be approximated as equal.

The DEM calibration algorithm should be tested again with more accurate baselines, which can be obtained from dynamic estimation. This would possibly expand the number of cases in which it converges and allow us to evaluate the possibility that the baselines accuracy improves with the number of satellite when employing such an algorithm. Including in the covariance matrix some level of correlation between SAR data from different satellites and restricting the available SAR data for one per orbit would make the simulation more realistic. It is possible that, by doing so, the SAR calibration would improve the baseline mainly for the time frame in which the SAR data was taken. This would still be a positive result since in SAR applications only the baseline between satellites during radar data acquisition interval matters.

The use of dynamic models in the estimation would also open new possibilities of exploiting the close proximity of the satellites. Many parameters affecting the orbital mechanics - for example, the air density and solar radiation intensity - are highly correlated for identical satellites flying at close distances. It is possible that by considering these parameters to be the same for every satellite, they could be more accurately estimated by processing the data from several satellites in a single filter, and more accurate baselines estimates could be achieved by consequence.

The proposed SAR synchronization scheme can be further tested and evaluated by implementing it in hardware. The first step would be to check if the assumption that phase drifts in the radar signal and in the reference GNSS signal are be proportional to each other if the signals originate from the same oscillator. This can be tested simply by implementing the up-conversion phases and monitoring the output signals. The following would be to effectively implement the scheme with two GNSS receivers and performing a test using GNSS signal simulators. In a controlled environment, the output radar signal, the simulated baselines and the reference GNSS signals can be monitored and the phase error estimated from the data can be compared to the expected results from the error analysis. The multipath effects should also be evaluated in a laboratory environment and reduced to an acceptably low level.

If the proposed synchronization scheme turns out to be effective in a real scenario - as predicted in this thesis - it could be a important step towards reducing the cost and complexity of bi-and multistatic SAR systems and enabling ambitious mission concepts with several SAR satellites flying in formation.

Bibliography

[ADM10] Ardaens, Jean-Sébastien, Simone D'Amico and Oliver Montenbruck: *Flight Results from the PRISMA GPS-Based Navigation.* In *5th ESA Workshop on Satellite Navigation Technologies, NAVITEC*, Noordwijk, Netherlands, January 2010.

[Aut84] Auterman, J. L.: *Phase stability requirements for bistatic SAR.* In *Proc. IEEE Nat. Radar Conf.*, pages 48–52, Atlanta, USA, March, 1984.

[BV] Braubach, Harald and Michael Voelker: *Method for drift compensation with radar measurements with the aid of reference radar signals.* US Patent 7,209,072, 24 April 2007.

[CW05] Cumming, I. G. and F. H. Wong: *Digital Processing of Synthetic Aperture Radar Data. Algorithms and Implementation.* Artech House, Boston, London, 2005.

[ece] *ICEYE SAR DATA.* `https://www.iceye.com/sar-data`. accessed: May 16, 2020.

[GAB+12] González, Jaime Hueso, John Mohan Walter Antony, Markus Bachmann, Gerhard Krieger, Manfred Zink, Dirk Schrank and Marco Schwerdt: *Bistatic system and baseline calibration in TanDEM-X to ensure the global digital elevation model quality.* ISPRS Journal of Photogrammetry and Remote Sensing, 73:3–11, 2012.

[Gro13] Groves, Paul D: *Principles of GNSS, inertial, and multisensor integrated navigation systems.* Artech house, 2013.

[HWC12] Hofmann-Wellenhof, B., Lichtenegger H. and J. Collins: *Global positioning system: theory and practice.* Springer Science & Business Media, 2012.

[HWLC97] Hofmann-Wellenhof, B., H. Lichtenegger and J. Collins: *GPS, Theory and Practice.* Springer-Verlag Wien, New York, 1997.

[JDM+09] Jäggi, Adrian, R Dach, O Montenbruck, U Hugentobler, H Bock and G Beutler: *Phase center modeling for LEO GPS receiver antennas and its impact on precise orbit determination.* Journal of Geodesy, 83(12):1145–1162, 2009.

[KH03] Kedar, S., Hajj G.A. Wilson B.D. and M.B. Heflin: *The effect of second order GPS ionospheric correction on receiver positions.* Geophysical Research Letters, 30(16), 2003.

[Klo95] Klobuchar, J. A.: *Ionospheric effects on GPS.* Global Positioning System: theory and applications, 1, 1995.

[KM06] Krieger, G. and A. Moreira: *Spaceborne bi- and multistatic synthetic aperture radar: potential and challenges.* IEE Proc. Radar Sonar Navig., 153(3):184–198, June 2006.

[KMBV05] Kroes, Remco, Oliver Montenbruck, William Bertiger and Pieter Visser: *Precise GRACE baseline determination using GPS.* GPS Solutions, 9:21–31, 2005.

[KMF+07] Krieger, G., A. Moreira, H. Fiedler, I. Hajnsek, M. Werner, M. Younis and M. Zink: *TanDEM-X: a satellite formation for high-resolution SAR interferometry.* IEEE Trans. Geosci. Remote Sens., 45(11):3317–3341, November 2007.

[Kro06] Kroes, Remco: *Precise relative positioning of formation flying spacecraft using GPS.* PhD thesis, Delft University of Technology, Delft, Netherlands, April 2006.

[KY06] Krieger, G. and M. Younis: *Impact of oscillator noise in bistatic and multistatic SAR.* IEEE Geosci. Remote Sens. Lett., 3(3):424–428, July 2006.

[KZM+18] Krieger, Gerhard, Mariantonietta Zonno, Josef Mittermayer, Alberto Moreira, Sigurd Huber and Marc Rodriguez-Cassola: *MirrorSAR: A Fractionated Space Transponder Concept for the Implementation of Low-Cost Multistatic SAR Missions.* In *EUSAR 2018; 12th European Conference on Synthetic Aperture Radar*, pages 1–6, Aachen, Germany, June 2018. VDE.

[Lea87] Lear, WM: *GPS navigation for low-earth orbiting vehicles.* NASA Lyndon B. Johnson Space Center, Mission planning and analysis division, 1st revision, NASA, 1987.

[MG00] Montenbruck, O. and E. Gill: *Satellite orbits: models, methods, and applications.* Springer Verlag, Heidelberg, 2000.

[MGFY+09] Montenbruck, Oliver, Miquel Garcia-Fernandez, Yoke Yoon, Steffen Schön and Adrian Jäggi: *Antenna phase center calibration for precise positioning of LEO satellites.* GPS solutions, 13(1):23, 2009.

[MPY+13] Moreira, A., P. Prats-Iraola, M. Younis, G. Krieger, I. Hajnsek and K. P. Papathanassiou: *A tutorial on synthetic aperture radar*. IEEE Geoscience and Remote Sensing Magazine, 1(1):6–43, 2013.

[MR] Montenbruck, O. and C. Renaudie: *Phoenix-S/-XNS Performance Validation*. Technical Report GTN-TST-0120, German Space Operations Center (GSOC), DLR.

[MvYV07] Montenbruck, O, PWL vanBarneveld, Y Yoon and Visser: *GPS-based precision baseline reconstruction for the TanDEM-X SAR-formation*. 2007.

[Poz12] Pozar, David M: *Microwave engineering*. Wiley, 2012.

[RC12] Rodriguez-Cassola, M.: *Bistatic Synthetic Aperture Radar Data Processing*. PhD thesis, DLR Technical Report, Oberpfaffenhofen, Germany, 2012.

[RCPIZ+17] Rodriguez-Cassola, M., P. Prats-Iraola, M. Zonno, M. Nannini, P. López-Dekker, B. Carnicero-Dominguez, B. Rommen and A. Moreira: *End-to-end performance analysis of companion SAR missions*. In *2017 IEEE International Geoscience and Remote Sensing Symposium (IGARSS)*, pages 153–156, Fort Worth, USA, July 2017. IEEE.

[RCPS+12] Rodriguez-Cassola, M., P. Prats, D. Schulze, N. Tous-Ramón, U. Steinbrecher, L. Marotti, M. Nanninni, M. Younis, M. Zink, A. Reigber, P. López-Dekker, G. Krieger and A. Moreira: *First bistatic spaceborne SAR experiments with TanDEM-X*. IEEE Geosci. Remote Sens. Lett., 7(1):108–112, January 2012.

[SCFD16] Setty, Srinivas J, Paul J Cefola, Hauke Fiedler and Juan Felix San Juan Diaz: *Attributes affecting the Accuracy of a Batch Least Square Orbit Determination using Semi-analytical Satellite Theory*. In *Proc. of the Maui Optical and Space Surveillance Technologies Conference*, September 2016.

[TK98] Teunissen, P.J.G. and A. Kleusberg: *GPS for Geodesy*. Springer, 1998.

[Val01] Vallado, David A: *Fundamentals of astrodynamics and applications*, volume 12. Springer Science & Business Media, 2001.